UNIVERSITY OF OKLAHOMA

GRADUATE COLLEGE

ANALYSIS AND EFFECTS OF AIRFLOW DISTRIBUTION ON LASER POWDER BED FUSION

A THESIS

SUBMITTED TO THE GRADUATE FACULTY

in partial fulfillment of the requirements for the

Degree of

MASTER OF SCIENCE

By REED SMITH

Norman, Oklahoma

2025

ANALYSIS AND EFFECTS OF AIRFLOW DISTRIBUTION ON LASER POWDER BED FUSION

A THESIS APPROVED FOR THE

SCHOOL OF AEROSPACE AND MECHANICAL ENGINEERING

BY THE COMMITTEE CONSISTING OF

Dr. Yingtao Liu, Chair

Dr. Shivakumar Raman, Co-chair

Dr. Jingyao Dai

Dr. Yijie Jiang

Acknowledgments

The adventure of earning a B.S. and M.S. in Aerospace Engineering in 51 calendar months is one that will stick with me forever – both for the memories and lasting knowledge, and the years I am sure it took off me. To thank every person who had an impact on me would require another 50+ pages of writing; however, there are some who must be highlighted.

First, I would like to acknowledge all the professors in the OU College of Engineering and specifically in the School of Aerospace and Mechanical Engineering. I may have been frustrated with you some days, but as a working alumnus, I can say your teaching provided me with knowledge that will fuel my life ahead and has taught me to tackle any problems that come my way.

To Drs. Jingyao Dai and Yijie Jiang, for volunteering to join my committee and selflessly lending their help and guidance to me. You have both demonstrated your strong dedication to innovation and education through your actions.

To Drs. Yingtao Liu and Shivakumar Raman, for believing in me as a young sophomore. Allowing me to join a multimillion-dollar research project and pursue my research interests with your full support. Your trust and guidance allowed me to pursue my passions and research innovative ideas that few college students or industry professionals will ever do.

A special thank you to Sean Brownlee, who selflessly dedicated many hours of his time to helping me design and troubleshoot the electrical aspects of this airflow device. Your voluntary initiatives to research and find solutions to problems I was facing helped me learn and stay on pace more than you can imagine.

To my engineering school “team” of Erik Winkeljohn, Quy Ninh, and Izzack Hernandez, for spending countless nights staying up late completing homework, locking ourselves in study rooms for 10+ hours to complete projects, and for helping me have fun through the stressful journey of engineering. Without a strong group, engineering school can be impossible – I was lucky to find mine early on.

To my family, who provided me with the wisdom to tackle college head-on and position myself for success. It was your guidance that I watched as the youngest sibling that led me to this point today. You have been my biggest role models since the very beginning.

To my parents, who believed in me from day one. Supporting me in all the adventures and providing me the ability to chase my dreams. There is truly no amount of thanks I can give for the support I felt throughout my time at OU and in my life.

And, finally, to my wife, Grace. We met just as school was ramping up into junior year, and you stuck with me through all the long nights, stressful tests, and this 68-page thesis. Your selfless and loving support has kept me going through it all. I know you are excited to finally have my full attention every night and not have to hear about homework, tests or papers – and trust me I am too. I love you so much and could not think of anyone else I would’ve wanted by my side during this journey.

This thesis is dedicated to the pursuit of engineering and innovation. True progress demands courage to venture into the unknown - the very essence of aerospace engineering.

Table of Contents

List of Figures

List of Tables

Abstract

Advanced manufacturing has experienced a rapid increase in modern industrial practices over the last few decades. At the forefront of this growth is metallic 3D printing, specifically, laser-powder bed fusion (LPBF). The advanced and sensitive nature of LPBF requires fine-tuning of process variables – one of those being argon gas distribution throughout the build chamber. The objective of this thesis is to discuss the design and measurement data obtained from an airflow measurement device installed within the build chamber of a General Electric (GE) Concept Laser M2 Series 5 metal 3D printer – a pilot study into the effects of airflow on the LPBF process. The device collected 1,000 data points across the volume directly above the surface of the build plate at three airflow velocities: low (1.95 m/s), nominal (2.05 m/s), and high (2.15 m/s). The airflow device was constructed from simple 3D printer hobby materials. The pitot tube and mechanical components were controlled using external computers and original code written for this data acquisition. The testing focused on 4 critical zones: front edge of the plate, just inside the front edge of the plate, the centerline of the plate and the trailing edge of the plate. These measurement points produced figures that showed channels of ideal airflow and areas of poor distribution throughout the chamber. The airflow data was compared to previously measured mechanical strength data to determine the ideal printing conditions. Overall, the pilot study found that airflow differences did not result in notable print quality differences; however, they presented enough evidence to suggest ideal conditions and plate placements for sensitive print requirements. The purpose of these results is to set a foundation for future research into airflow conditions and do not provide any concrete conclusions.

Chapter 1. Introduction

1.1 The Rise of Advanced Manufacturing

The rapid advancement in technology over recent decades has profoundly changed our daily lives. A particularly transformative development is the emergence of advanced manufacturing, especially additive manufacturing through 3D printing. Although often overlooked, manufacturing has a profound influence on numerous aspects of life, as people rarely consider the makers and processes behind the products they use. 3D printing, once confined to laboratories and industry, now enables individual users to easily manufacture items at home, thanks to affordable machines that require little training. This shift parallels the democratization of technology that has been seen with personal computers.

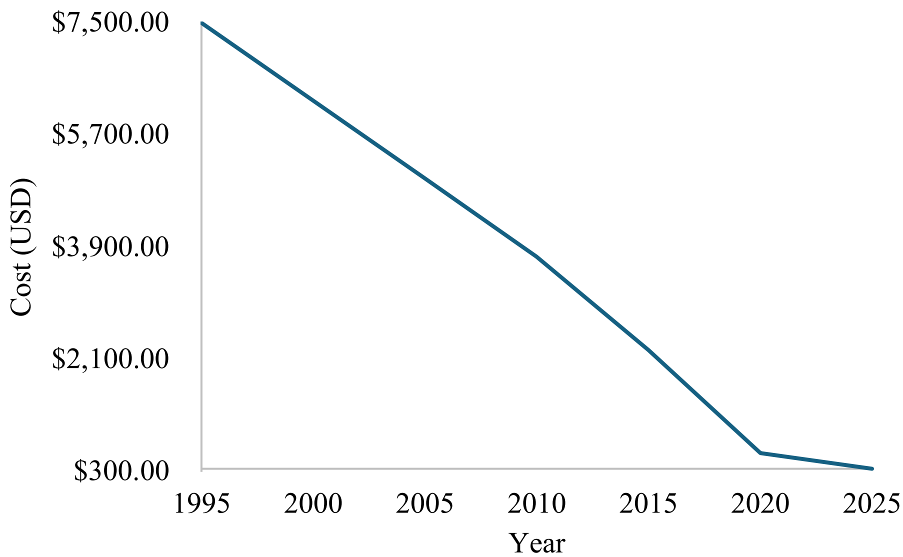

Figure 1. Cost of 1 kg print using 3D metallic printing over the last 30 years [1]

Figure 1 above illustrates the significant decline in the average cost to 3D print one kilogram of metallic components over the past thirty years. The last five years have experienced a decreased rate in price reduction, partially due to optimized processes and global supply chain issues [1]. Simple, conventional filaments, such as polylactic acid (PLA), used in generic 3D printing, have evolved into application-specific materials, engineered for cost, performance, and mechanical properties. These advanced filaments include metallic alloys, composites, and, recently, bio-matter, which can be utilized for critical components in various applications, including aerospace and defense, biomedical, dental, and automotive [2]. This has led to a global market increase, with a more than two-fold value increase every five years, as shown in Figure 2, to help supplement the supply-chain challenges faced in standard manufacturing processes [1].

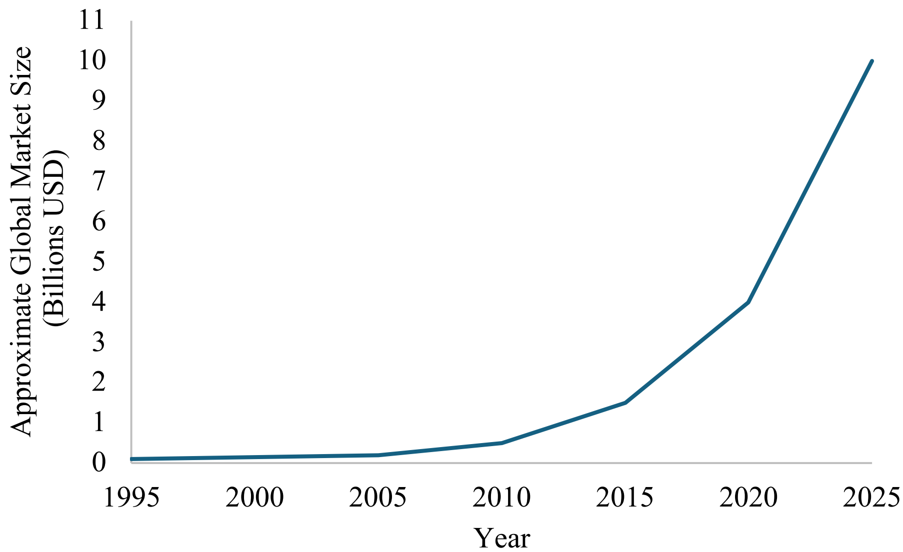

Figure 2. Global market size (billions USD) of 3D metallic printing over the last 30 years [1]

These new manufacturing capabilities enable reverse engineering, rapid prototyping, design modifications and mass-reproducible production thereby shortening the time required to design and produce a component [3].

1.2 Laser Powder Bed Fusion

With the growing field of advanced manufacturing practices, laser powder bed fusion (LPBF) has established itself as a cornerstone of modern research interests [4]. This process utilizes fine metallic powders as the base material, whereas polymer 3D printers typically use extruded plastic filaments. These powders consist of fine metallic particles, with an average diameter of 30 µm, or approximately half the width of a single human hair [4]. These particles are spread evenly in a thin layer across a build plate by a metallic or rubber re-coater blade, after which a high-power energy source, a laser in this case, is used to fuse particles at desired locations, set forth by the digital model [4]. After this, the layer is given time to cool and regulate before the process is repeated, using layer thicknesses of 20-100 µm, depending on desired print time and surface finish [4].

Figure 3. Ti-6Al-4V LPBF printing powder [5]

1.3 Argon Distribution

To optimize LPBF print results, airflow is distributed throughout the build chamber during the fusion process [6]. Due to the high reactivity of the metallic powders, inert gases, often argon or nitrogen, are used, much like the shielding gases used in welding [7]. Inert gases, which do not react with other materials, reduce the effects of oxidation on the components, which can hamper surface quality and mechanical properties [6]. It also addresses another major issue known as spatter, or contacted powder expressed into the air from laser impact, which is frequently experienced in LPBF [8]. Extreme forces projected onto the powder during the laser-directed fusion process cause particles to become airborne, resulting in a pollution cloud that forms around the build plate surface [6]. These pollutant particles, or spatter, spread elsewhere on the surface of the build plate and in the air, resulting in secondary fusion and compromised print quality [8]. This introduces surface defects and reductions in microstructural and mechanical properties in the finished print [9]. Particles can also remain in flight long enough to be struck by subsequent laser pulses while airborne, refracting the laser beam away from the surface and disturbing the fusion process on the surface of the build plate [8]. Figure 4 below showcases the spatter cloud formed around the fusion point and the secondary dispersion effects.

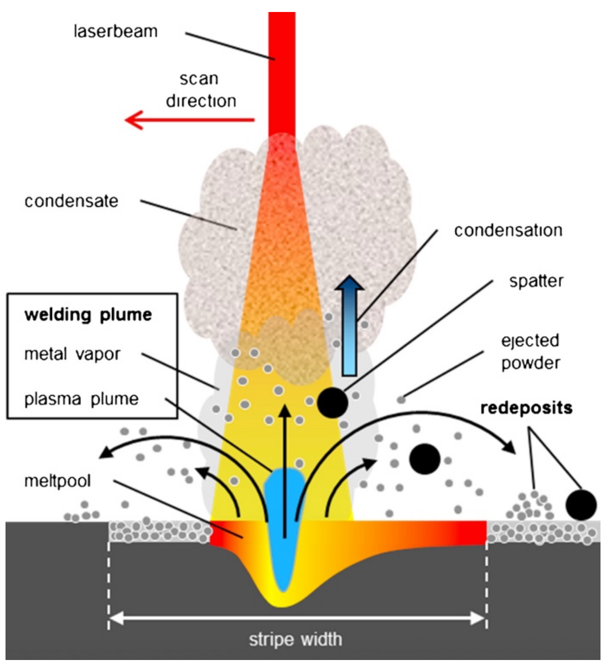

Figure 4. Spatter pollutants produced during the LPBF process [10]

To mitigate the effects of spattering, the chamber gas flow, commonly argon, is carefully directed to help carry the pollutant particles away as an exhaust gas [7]. The evacuation of these by-products is designed to increase the build rate and improve the cleanliness of the melting processes during fusion [7]. By optimizing these characteristics, defects such as porosity, inclusions, cracks, surface issues, and oxidation can be significantly reduced, thereby improving the surface, mechanical, and microstructural properties [9].

1.4 Advanced Manufacturing at the Sooner Advanced Manufacturing Laboratory

Located in Norman, Oklahoma, the Sooner Advanced Manufacturing Laboratory (SAML), in conjunction with the University of Oklahoma and the Oklahoma Aerospace & Defense Innovation Institution (OADII), specializes in groundbreaking manufacturing practices and processes to advance the efforts of the United States Department of Defense (DoD) and the United States Department of the Air Force (USAF). The SAML, which is supported through Air Force Research Lab (AFRL) grants and other government/commercial contracts, works to develop new, cutting-edge manufacturing techniques using additive manufacturing equipment, such as two General Electric (GE) Concept Laser M2 Series 5 metal 3D-printers, and advanced pre- and post-processing equipment to manufacture critical components.

Figure 5. General Electric (GE) Concept Laser M2 Series 5 metal 3D printer

Due to the underdeveloped or non-existent engineering technology, such as modern computer-aided design (CAD) and finite element analysis (FEA) software, used during the design and manufacturing processes of many aircraft still in use today, recreating and re-engineering new components requires extensive time and effort. By utilizing state-of-the-art advanced manufacturing processes, the SAML aims to reduce maintenance and repair times from multiple months or years to a few weeks. The technology designed and analyzed in this thesis is part of the research being conducted at the SAML and is protected under CUI regulations; therefore, specific data points and design features have been omitted to ensure that proper security protocols are met.

1.5 Problem Statement and Thesis Outline

As stated previously, the ability to control variables within the advanced manufacturing process is essential, not only to ensure proper results but also to achieve optimal replicability for future uses. A substantial issue faced by the SAML and other additive manufacturers is ensuring that argon gas flows evenly and consistently in terms of velocity and pressure over the build plate throughout the duration of the fusion process. To accurately address this issue, it is essential to first understand the raw flow characteristics of the airflow through the build chamber. To validate this, an airflow distribution measurement device was designed and constructed to take pressure measurements throughout the chamber, allowing velocity distribution maps to be generated, which highlight areas of concern. This thesis presents the design and testing of the device, providing and analyzing data received from the print chamber and supporting mechanical strength data to inform initial, pilot-study findings about ideal airflow practices and recommendations for future research.

Chapter 2. Reverse Engineering

2.1 Reverse Engineering at the SAML

Reverse engineering is a cornerstone of the SAML operations and a rapidly expanding and evolving focus of engineering, especially in the field of advanced manufacturing. Reverse engineering (RE) is formally defined by Cornell College of Law as, “a method or process of developing or manufacturing a known product [as] discovered through 'working backward', such as taking apart the known product” [11]. More simply put, it is the method of using a previously existing part to recreate a new one that is identical or improves on previous designs or issues. The aircraft components that the SAML receives are often without any technical data package or previous data on which the part was designed or manufactured. This is due primarily to two factors: 1. Parts received at the SAML are often retrieved from aging fleets, such as the B–52 Stratofortress, an aircraft that entered service in 1955, significantly before the integration of modern engineering practices; and 2. Many smaller components of these aircraft are manufactured by external contractors, which often experience a high turnover rate, making their manufacturer origins obsolete [12]. In these cases, the SAML must reverse engineer parts from scratch. This requires a complete component profile to be constructed by the SAML, including material composition, surface finish, previous manufacturing techniques and processes, coatings, and other relevant details. This data is then used to design and produce LPBF additively manufactured components, which can be replicated across facilities to recover supply chain slowdowns. To assist in the RE process, the SAML utilizes a range of sophisticated, modern equipment and tools to analyze parts. These include 3D scanners, X-ray and MRI technology, surface polishers and hardness testers, microscopes, electromagnetic testers, tensile and torsional testers, and cross-section slicers. These tools enable the creation of a comprehensive technical profile for a component before the redesign process.

2.2 Modern Reverse Engineering Technology

The SAML prides itself on utilizing state-of-the-art reverse engineering technology for both non-destructive and destructive inspection processes. These technologies provide rapid, cutting-edge results that not only reduce time and improve accuracy but also enable the collection of data that would otherwise be impossible to obtain by conventional practices. At the heart of the SAML RE operation and processes used for this research are 3D scanners, which enable high-accuracy and high-resolution imaging techniques.

2.2.1 Blue Light vs Laser

Modern 3D scanning technology is dominated by two methods: blue light and laser scanning [13]. These methods employ similar techniques and equipment but are applied to different scenarios and constraints. Both technologies can provide accurate and precise data points and must be chosen to fit the project's specific needs. Within the SAML, blue light scanning is the primary method; however, laser scanning is also employed for reverse engineering practices.

Blue light scanning technology utilizes structured blue light, typically LED, to project a preset pattern onto the surface of an object. As the projected light hits the surface of the object, it is affected by the geometry and therefore bends and deforms from the original pattern [13]. Cameras simultaneously measure these bends and deformations, transmitting the differences to software that can then recreate a digital image of the part [13]. This measurement method provides exact geometrical data and is less prone to ambient light and environmental effects than other light scanners [13]. Due to the structure of the light used, this method is best suited for small to medium applications within a close range, meeting the needs of most SAML work.

Laser scanners direct a laser beam towards the surface of an object and measure the time it takes for the beam to return to the device [14]. The time is then converted, considering the intensity of the laser beam, to determine the distance the part is from the scanner. Software then uses this data to recreate a digital image [14]. As a laser beam is less susceptible to environmental interference, it is more commonly used in larger applications over an extended range, where structured light would no longer be fully capturable [14].

With both methods, the final scans compile millions of data points that are collected and meshed using a point cloud, or a web of points interconnected by known distances [15]. Rapid innovation in the reverse engineering industry allows these scanners to obtain millions of data points in just a few seconds, providing rapid and precise scans [15]. Below is a table comparing the characteristics of blue light and laser scanners. It is essential to note that neither scanner is inherently “better” than the other for all applications, and the choice of device is highly dependent on specific environmental and project-specific requirements.

Table 1. Comparison of blue-light scanning technique vs laser [16][17]

Criteria	Blue – Light	Laser
Accuracy	High (± 0.005 mm)	Medium (± 0.02 mm)
Resolution	High – Fine details	Medium – Larger objects
Cost	$10K - $100K	$10K - $100K
Point Cloud Density	High – multi-million points	Medium – 100s of thousands to low millions of points
Limitations	Large objects, surrounding light conditions, surface/environment prep	Fine details, complex geometry, reflective surfaces

2.2.2 Keyence VL-700 Series

The foundation of SAML reverse engineering equipment is the Keyence VL-700 3D-Scanner, which is used to scan all removable and mobile parts received from the Air Force, as well as for in-house needs. The VL-700 uses a structured blue light system as discussed above [16].

Figure 6. Keyence VL-700 Series light projection measurement system [16]

Using the method of triangulation, connecting three known surface points to form a triangle, the Keyence obtains precise coordinate data from the surface of the component to an accuracy of ± 10µm [16]. The remaining key performance factors of the VL-700 are shown in Table 1 below.

Table 2. Keyence VL-700 Series performance factors [16]

Factor	Specification
Scanner Resolution	9 megapixels
Repeatability	± 2 µm
Point Cloud Density	9 million points/scan
Scan Time	30 s < t <10 min, depending on part size and geometry

Parts that require reverse engineering can be quickly scanned with the Keyence, providing millions of data points within minutes and a complete 3D digital image that can be manipulated and analyzed. These images enable the observation of surface qualities including coatings, scratches, voids and post-processing scars at high resolution. The scans are also used to obtain geometric data such as critical dimensions and angles. This data can then be directly inputted into CAD software to ensure geometric accuracy during the rebuild and redesign phase.

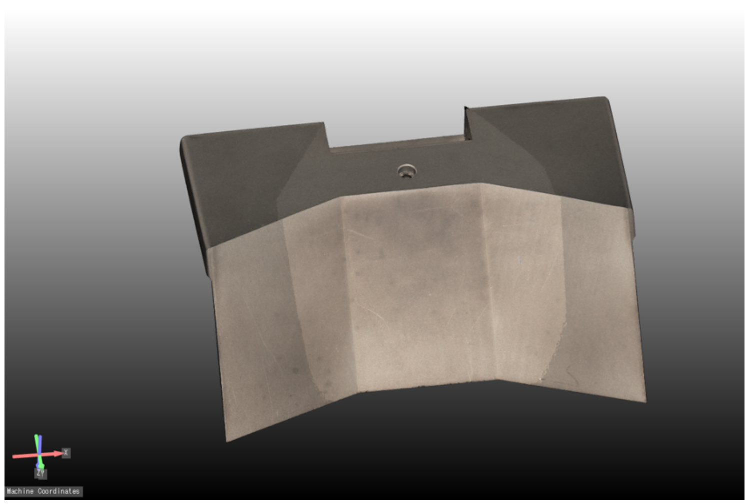

Figure 7. Keyence scanned 3D mesh image of the powder chamber component

Unfortunately, due to the nature of the scanning process, parts with high reflectivity, such as the chrome finishes found inside the print chamber, cannot be scanned raw as the reflected light results in holes in the scan. To mitigate this, an evaporative spray coating is used to matte the surface finish without ruining the part or hampering the geometric integrity of the scan.

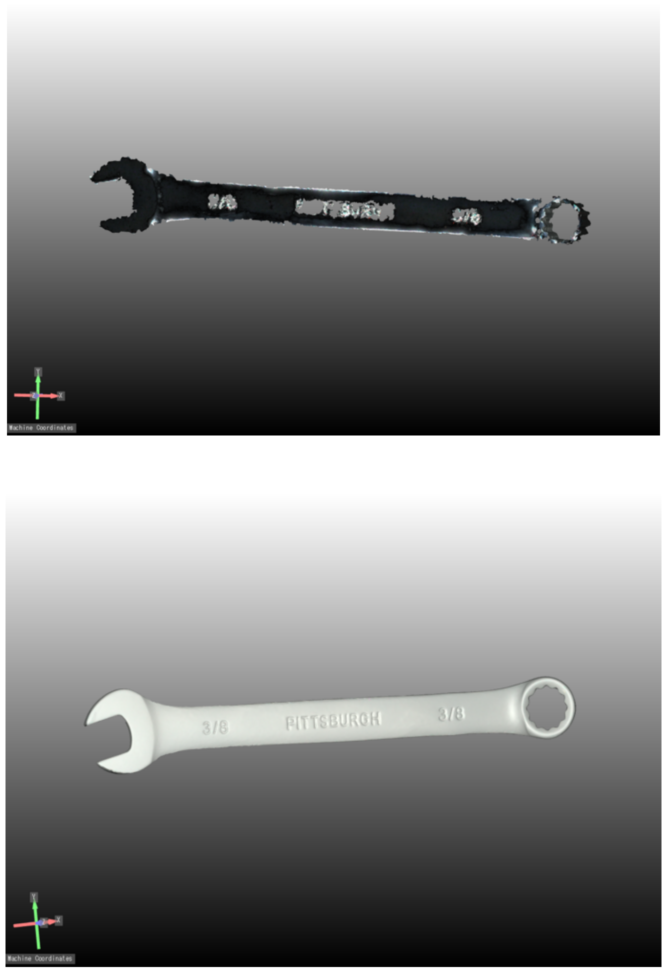

Figure 8. Comparison of surface finishes: chrome finish (top) vs matted finish using spray (bottom)

2.2.3 Handheld Scanners

When a part requires 3D scanning but cannot be removed from its existing installation or exceeds the size constraints of the Keyence platform, a handheld blue-light scanner can be used to obtain similar data points and images. At the SAML, a Revopoint MetroX Handheld Blue Light Scanner is used for all reverse engineering applications that fit these criteria.

Figure 9. Revopoint MetroX handheld blue-light scanner [17]

This scanner uses the same blue light techniques as the Keyence scanner and can capture a large field of data; however, due to this increased range and mobility, there is a noticeable drop in scan accuracy, decreasing resolution tolerance to that of ± 0.01mm [17].

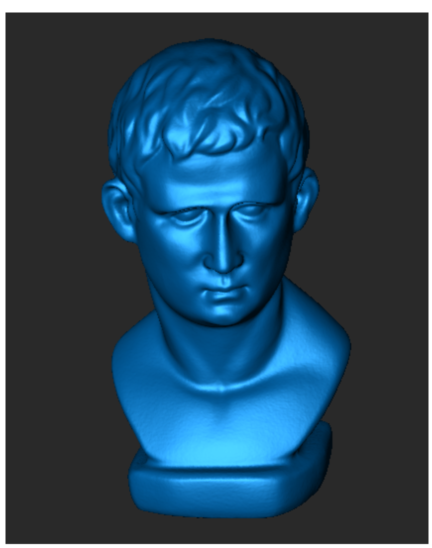

Figure 10. Completed 3D scan of a figurine utilizing the MetroX Handheld Scanner

Chapter 3. Design Phase

3.1 Initial Design Constraints

The initial design phase of the airflow measurement device required an in-depth reverse engineering process of the LPBF print chamber and its surrounding environment, as well as a preliminary analysis of the problem and the desired solution. Initial constraints that had to be considered during the design phase included chamber size and geometry, the coverage area of the pitot tube, operating within a sealed chamber, and the ability to install efficiently. Fortunately, the two printers used at the SAML are identical, except for powder used, making the design feasible for use in both. The available input and output sources in the chamber include only a 12-volt source, an Ethernet port, and a USB port. A total of 1,000 data points were desired at each airflow velocity across the build plate.

3.2 The Chamber

The build chamber of the GE Additive Concept M2 Series 5 LPBF printer is the primary location for all metallic 3D printing processes. The build chamber is where the fusion process occurs and is the primary focus of the airflow analysis. The chamber is sealed during operation to maintain the inert environment achieved by using argon infused during the pre-print process, resulting in a less than 0.01% O_2 concentration. The chamber is equipped with shielded observation windows that allow the fusing process to be safely viewed. During the pre- and post-print processes, the chamber can be shifted to the left side of the printer to allow for cleaning and removal of the build plate.

3.3 Build Chamber Operations

The purpose of the build chamber is to provide a sealed, safe environment for the fusion process of fine metallic powder using high-powered lasers to create a 3D-printed structure. To achieve this successfully, the chamber must have precise operations that are optimized and controlled to ensure the ideal mechanical properties of the completed builds. After the 245mm x 245mm solid stainless steel or titanium (dependent on powder being used) build plate is installed and prepared for the print process in the left-side chamber of the printer, it is shifted to the right side, into the formal build chamber. During the preparation process, the chamber is inerted by evacuating the oxygen supply and replacing it with argon gas. This helps ensure the preservation of virgin powder and prevents oxidation. The chamber is also heated to a temperature of roughly 200-250 °C, depending on the desired print quality, to prepare the build plate and chamber for ideal printing conditions, thereby preventing warping, cracking, and improving print adhesion.

After the initiation of the printing process, the build plate (placed in the center of the build chamber) is lowered by a set number of microns, determined before the print process to achieve the desired print results and layer height. At the same time, the powder chamber, directly adjacent to the plate, is raised by the same preset amount. A coater blade is then pushed from one side of the chamber, over the powder reservoir, and onto the build plate, ideally spreading the powder uniformly over the build plate. After this, dual lasers are used to fuse the desired geometry across the surface of the build plate, thereby fusing the top layer of powder to the layer below. This process is continued layer by layer until the final product is complete.

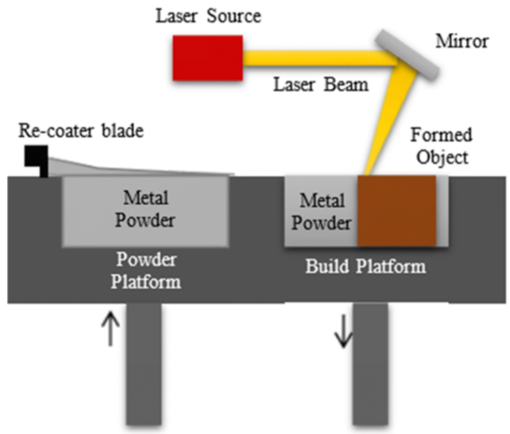

Figure 11. Generic LPBF build chamber process map [18]

During the fusion process, a flow of argon is distributed from the powder reservoir end of the chamber across the build plate and to an output port, where it is filtered and recirculated. As the argon enters the build chamber, it passes through a honeycomb structure to enhance laminar flow characteristics. This argon flow is used for two primary purposes: 1. Cooling the build plate to ensure uniform characteristics and minimize the effects of warping, and 2. Removing spatter particles that are expressed into the air during laser impact. Unfortunately, the factory-designed airflow is far from uniform, producing print defects and decreased mechanical properties in the finished components. The figures below illustrate the manufacturer's computational fluid dynamics (CFD) models, which demonstrate non-uniform airflow throughout the chamber, and the minor adjustments implemented in a second iteration to enhance performance. As can be seen, even with the improvements made in the second iteration, the airflow throughout the chamber remains less than ideal.

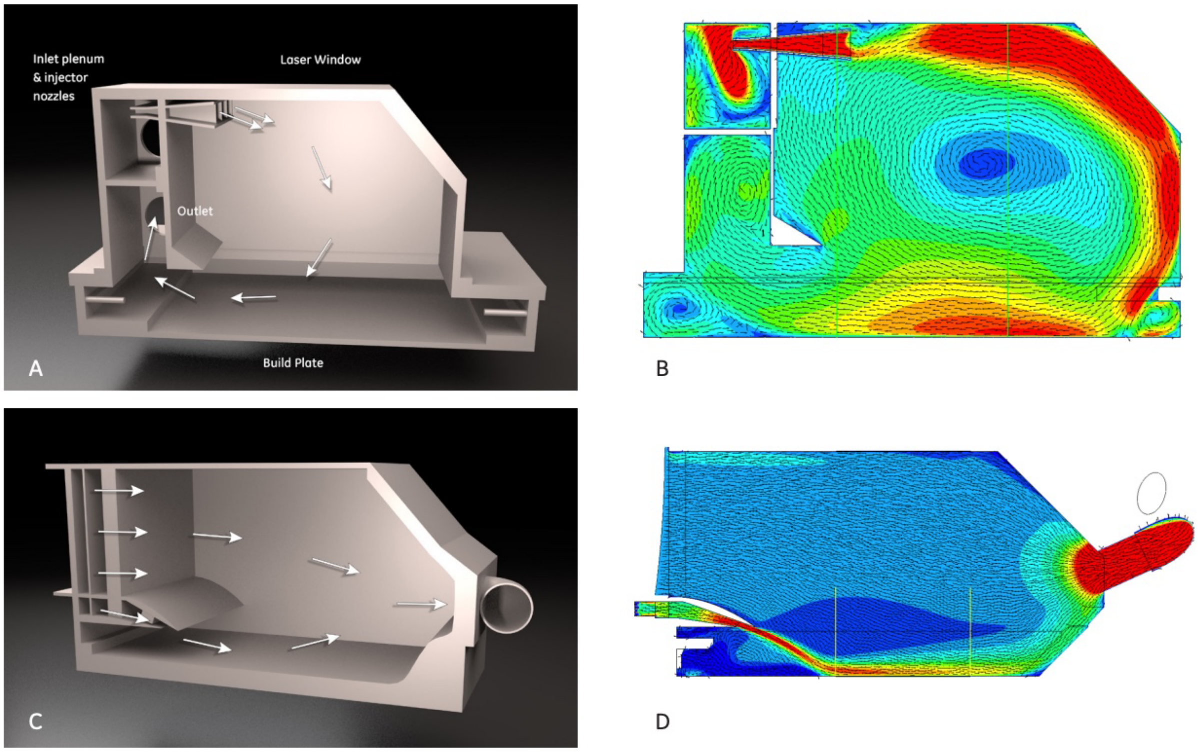

Figure 12. Manufacturer CFD of GE Additive Concept m2 Series 5 Dual Laser [10]

Iteration 1, pictures A and B, showcase a swirling flow which resulted in a strong vortex and static flow “eye” in the center of the chamber – a product of the same side inlet/outlet. The second iteration, pictures C and D, improved on this issue by pulling the airflow through the chamber and out the other side, in which the manufacturer claimed the airflow was more ideal for printing. Unfortunately, with the turbulent nature of the airflow and stagnant nature that remained in the CFD in iteration 2, only testing the properties of the printer in action could provide the trusted results. This resulted in the need for a certification process that this measurement device will provide.

3.4 Scanning the Print Chamber

To successfully design a device to measure argon airflow across the chamber, an accurate model of the print chamber was needed for rapid digital prototyping and simulation. To begin the chamber model design, a 3D scan needed to be acquired to ensure dimensional accuracy for the future CAD models. Due to the installed, tight geometric nature of the chamber, the MetroX Handheld Scanner was primarily used for this process. To obtain the most accurate and precise measurement data, bullseye stickers were utilized throughout the chamber's surfaces to provide more precise measurement reference points for the scanner. Initial scans produced splotchy images, resulting in more bullseye stickers being needed in the corners and complex areas. Further scans were taken to supplement the missing sections. The final scan required 45 minutes and collected over 60,000 measurement frames. The finished scan is shown in the figure below.

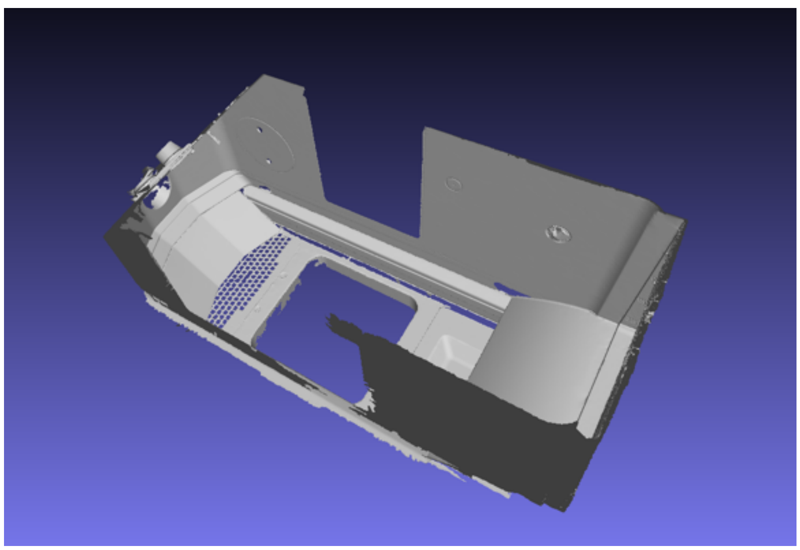

Figure 13. 3D scan image of the build chamber using the MetroX Handheld Scanner

This finished 3D scan mesh was imported into the MeshLab open-source software for analysis. Using this software, critical dimensions and angles were measured for use in recreating the chamber in a CAD model. Other removable parts were scanned using the Keyence VL-700 Desktop scanner. Parts such as the removable powder cover plate were removed from the chamber and scanned, as shown previously in Figure 7. These parts were then analyzed using the built-in Keyence software, similar to MeshLab, and prepared for CAD modeling.

3.5 Recreating the Chamber in SolidWorks

Upon completion of all scanning measurements, the newly acquired digital models were analyzed using dimensional analysis to obtain all necessary geometric data. This included data such as height, width, and depth, as well as angles of the chamber interior. With this data, the interior of the print chamber was recreated using SolidWorks CAD software. Figure 14 below is the completed print chamber CAD model that was used to assist in the design and modeling of the final measurement device.

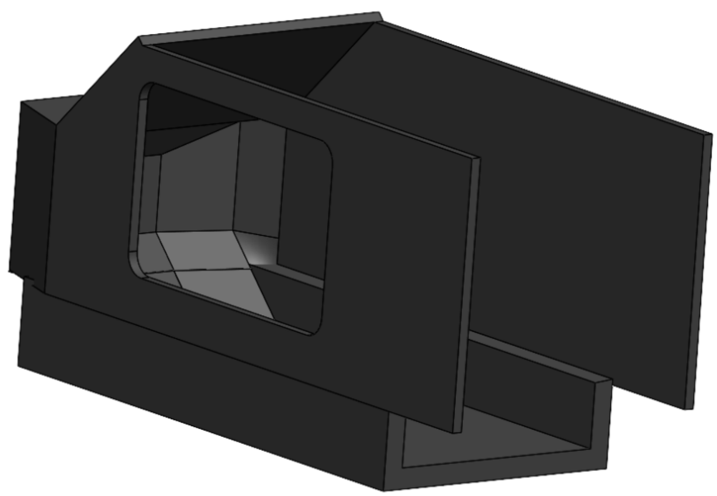

Figure 14. SolidWorks CAD assembly of the print chamber

Having a reverse-engineered digital model of the chamber enabled CFD analysis and device modeling to occur digitally within the chamber, without the need to manufacture any components or modify the existing chamber. This allowed for rapid prototyping with confidence of fit and functionality.

3. 6 Iteration 1 of Airflow Measurement Device

The first iteration of the airflow measurement device provided a proof of concept and identified initial design constraints, which included chamber size, restricted access to the chamber during the airflow process due to the inerting of the chamber, chamber door size, and desired autonomy of the device. After discussion and initial prototyping, it was determined to eliminate the 3-dimensional motion from the design. This would mean the device was only autonomously operable in the X-Y plane, which, for the purposes of this testing, was considered the vertical frame across the width of the chamber. This would require the device to be manually moved from each of the 10 Z-increments to the next, resulting in the inert seal in the chamber to be broken. The initial CAD of the device is shown below.

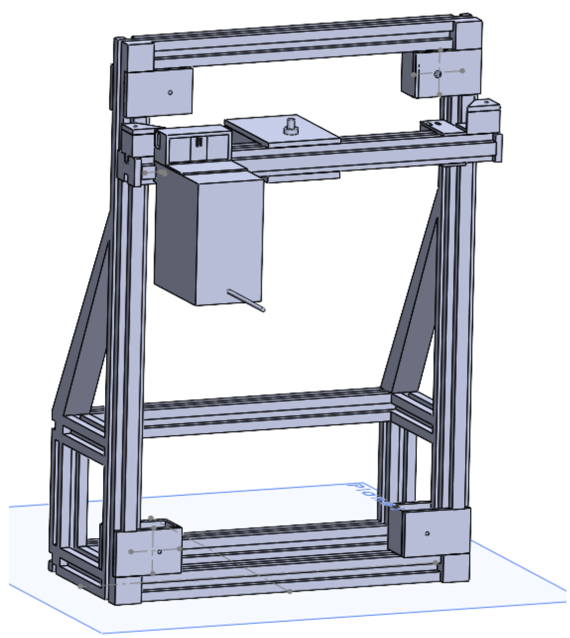

Figure 15. Initial CAD assembly of the measurement device

As seen in the figure above, the foundational frame of the device, its frontal frame, was also the point of X-Y plane motion. This resulted in the pitot tube holder, mounted on the front of the device's crossbar, producing a downward moment, causing the device to fall forward in initial functionality testing. To counter this, the rear electronics cage was increased in size; however, due to size constraints, counterweights had to be placed to supplement and cancel out moments.

3.7 Final Iteration

The final iteration looked to optimize the sizing characteristics while also focusing on the electronic and mechanical needs of the device. The final assembly within the chamber is shown below.

Figure 16. Final airflow measurement device fully assembled in the build chamber (frontal view)

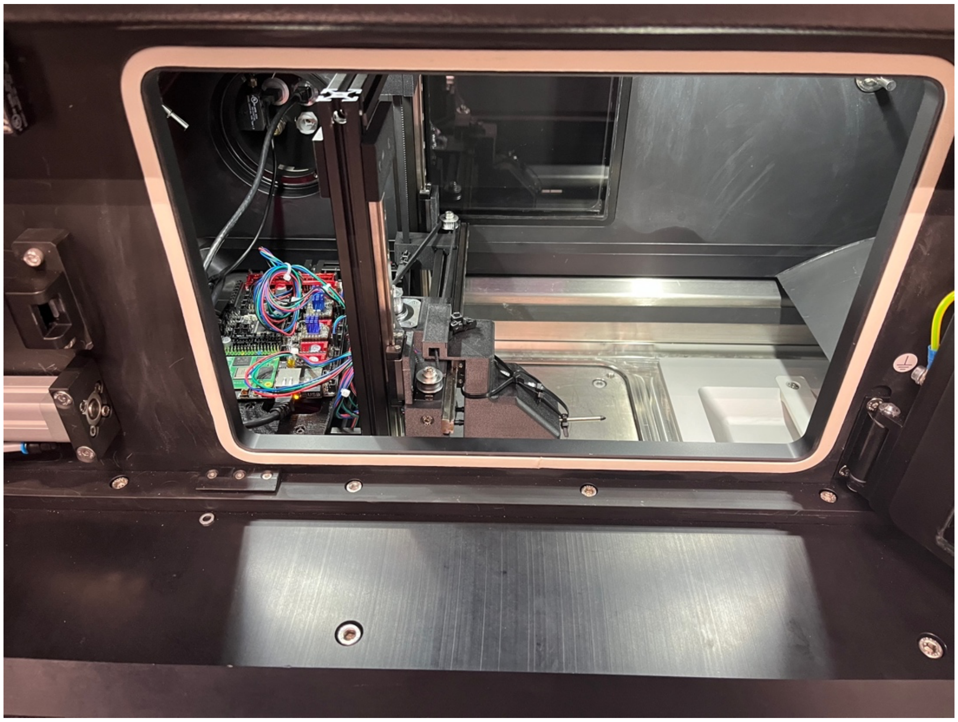

Figure 17. Final airflow measurement device fully assembled in the build chamber (side view)

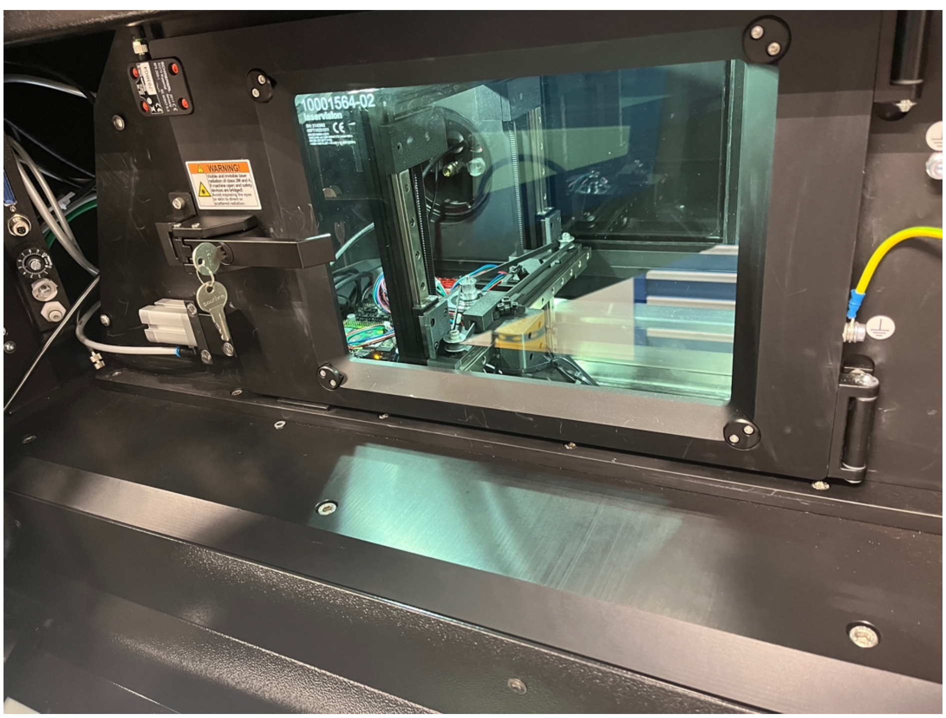

Figure 18. Final airflow measurement device fully assembled in the build chamber (sealed view)

The final components of the device consisted of an 80mm x 80mm T-slot extrusion bar and ABS Glass Fiber 3D-printed motor boxes, gear boxes, pitot tube holder, and electronic bay trays. The motors were NEMA-17 Bipolar Stepper motors from StepperOnline. The linear rails, gears and rubber timing belts were common hobby items purchased from a 3D-printing assembly set. The motors were controlled by a Bigtree Tech Manta M8P and Raspberry Pi connected to an external computer via an Ethernet cable with a 12-volt power source also attached. The pitot tube was connected to a LabJack T7-Pro via a pitot-tube converter. The LabJack served as the primary data-acquisition system and was connected to and powered by a secondary external computer via a USB cable.

3.8 Integrating Airflow Measurement and Motor Control

All wiring, both for power and data acquisition, was connected using a built-in power port provided in the print chamber, allowing for the chamber to remain sealed during the entire testing process. All tests were conducted using a pitot-tube that provided voltage data to a LabJack T7-Pro data acquisition device. The LabJack then transmitted all data to a connected computer, which executed a Python script that converted the voltage data to a corresponding pressure and velocity value. The pressure was determined by comparing the ratio of the measured voltage to the maximum voltage (5V in the case of LabJack) and then comparing it to the base pressure measured in the chamber by the Python script prior to initiating airflow [19]. The pressure data was then converted to velocity using Bernoulli's equation, as shown below

$$V = \sqrt{\frac{2\Delta P}{\rho}} \tag{1}$$

The Python script then saved each measurement point in a CSV file in the format of "Data Point, Voltage, Pressure, Velocity".

The device was mechanically controlled via Klipper firmware using the Klippie interface and Mainsail OS. G-Code maneuvered the device through its scan cycle, hitting all 100 points sequentially (a 10x10 matrix). The G-Code provided a 3-second delay after reaching each scan point to allow any airflow disturbances to be regulated. A full 100-point scan cycle was completed for each airflow condition. The device and code were then reset, the airflow was changed to the next condition, and the next scan cycle was initiated.

Chapter 4. Testing and Data Acquisition

4.1 Testing Parameters

The testing parameters were developed to simulate normal print conditions used at the SAML. This included replicated inert gas levels by fully inerting the chamber with argon beforehand, achieving O_2 levels less than 0.01%, installing the build plate and sensors used during a typical print, and using three air flow speed benchmarks: 1.95 m/s (low), 2.05 m/s (nominal), and 2.15 m/s (high).

4.1.1 Low Airflow

Low airflow speed for the purpose of this testing is considered 1.95 m/s, or 6.40 ft/s. This is regarded as the low speed used for SAML prints when necessary.

4.1.2 Nominal Airflow

Nominal airflow for the purpose of this testing is considered 2.05 m/s, or 6.73 ft/s. This is regarded as the nominal and common speed used for SAML prints.

4.1.3 High Airflow

High airflow speed for the purpose of this testing is considered 2.15 m/s, or 7.05 ft/s. This is regarded as the high speed used for SAML prints and is more commonly referred to as compared to low speed.

4.2 Testing

As the measurement device was not equipped with Z-axis autonomous motion capabilities, it had to remain at each Z-increment until manually repositioned. As the chamber was fully inerted for each test, it was decided to run a full test at low, nominal, and high airflow at each Z-increment before unsealing the chamber to reposition the device. A full 100-point scan was completed at each Z-increment (1-10) at each airflow condition (L, N, H), with increments 1, 2, 5, and 10 being measured twice, and data points averaged due to projected critical measurement zones identified from company CFD data. The decision for these critical zones will be discussed in the results section. After all three conditions were scanned at a Z-increment, the chamber was unsealed, and the device was moved to the next position, where the process was repeated until all ten positions were completed. The scanning process was spread across two days.

4.3 Mechanical Testing

To complete the comparative analyses necessary to confirm ideal airflow conditions, mechanical testing of additively manufactured specimens was conducted at each airflow condition across the build plate. These specimens were printed from a titanium alloy, Ti-6Al-4V, which is an alloy containing aluminum and vanadium. Ti-6-4 is recognized for its low density yet high strength and corrosion resistance, making it an ideal material for aerospace and defense applications [20]. These specimens were printed using the three airflow conditions and subsequently tested using a tensile testing device to measure the ultimate and yield tensile strengths (UTS and YTS, respectively). These prints and tests were conducted by Joshua Hall of the University of Oklahoma and the SAML in collaboration with this project to identify optimal printing conditions. Mr. Hall's data will be frequently referenced in this thesis as it provides mechanical strength data needed to complete the comparative analysis of the airflow [21].

4.3.1 Printing of Test Specimens

Eighty-one (81) identical dog-bone specimens were vertically printed in a 9x9 matrix formation across the build plate. The specimens were printed with a numeric label on the top side

(1-81) to help identify their location for analysis. The specimens were printed using Ti-6-4 powder and were all post-treated using the same processes.

4.3.2 Machining of Specimens

After printing, the specimens were all removed from the build plate using an Electrical Discharge Machine (EDM). They were then machined using an equation-driven lathe, which is used for research purposes at the SAML, providing micron-level geometric precision across each, thanks to the work of Mr. Sean Brownlee. These specimens were printed and machined into a dog-bone shape in accordance with ASTM E8, as shown in the figure below [22].

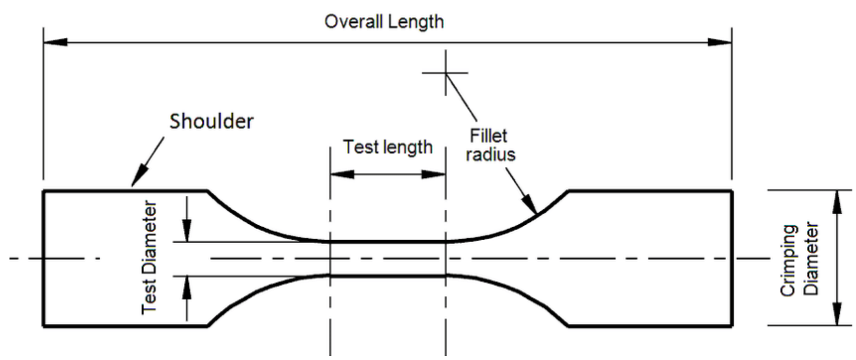

Figure 19. Typical dog bone shape used for tensile testing [23]

4.3.3 Tensile Testing of Dog Bones with Instron

The dog bone specimens were individually tensile tested using an Instron Tensile Tester to measure the UTS and YTS, adhering to ASTM standards E8 [22]. Testing was performed on all eighty-one (81) specimens from each airflow condition and recorded by specimen number and corresponding strength (MPa).

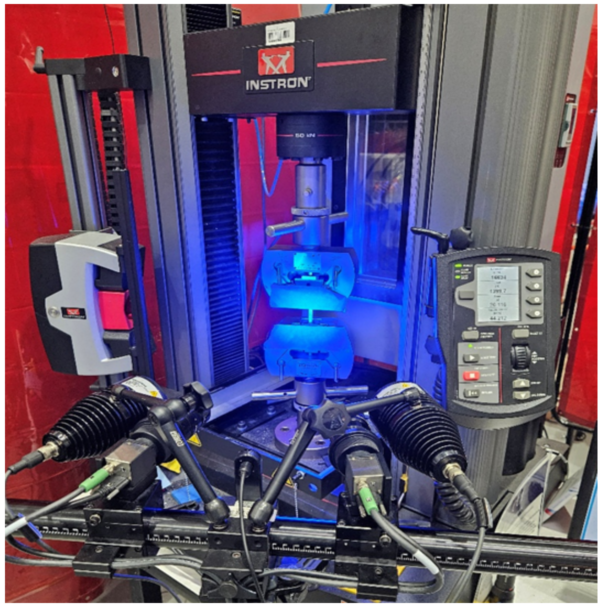

Figure 20. Instron Tensile Tester set-up at the SAML [21]

4.4 Airflow Statistical Analysis

The final side-by-side comparison of the airflow data will be analyzed using statistical analysis. This will allow for direct comparison using quantitative data. Mean, standard deviation, and maximum value will be recorded from the four critical zones. The mean of the data will be calculated using the following formula:

$$\bar{y} = \frac{1}{n}\sum_{n=1}^{n} a_i \tag{2}$$

where n is the number of samples (100 per plane) and a_i is the airflow velocity at each sample point. The standard deviation will be calculated using the following formula:

$$\sigma = \sqrt{\frac{\Sigma(y - \bar{y})^2}{N}} \tag{3}$$

where σ is the standard deviation, y is an airflow data point value, $\bar{y}$ is the previously calculated mean and N is the number of samples (100 per plane). The maximum value is simply found as the highest velocity measurement within the plane data.

Chapter 5. Results and Analysis

The airflow scans were successfully completed at all ten increments at the three velocity conditions. The results are shown in the three figures below. The figures showcase the full 1000-point scan data across the entirety of the 3D volume above the build plate. Areas of darker blue are areas of lower airspeed, while areas of red are higher velocities. As the Z planes are stacked on each other, the color darkness builds on itself. Due to this, the planes will be analyzed individually in the following sections.

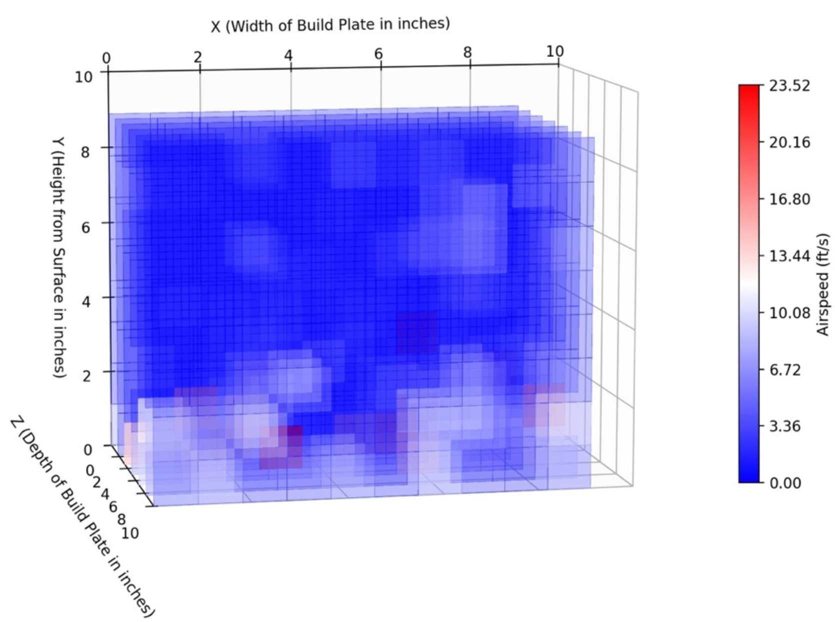

Figure 21. 3D airflow distribution across build plate (nominal flow)

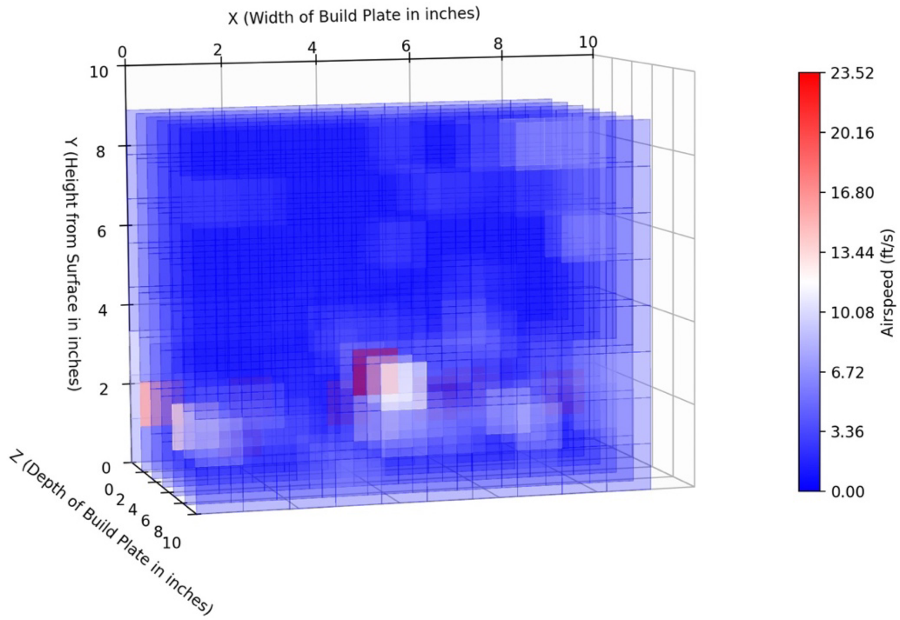

Figure 22. 3D airflow distribution across build plate (low flow)

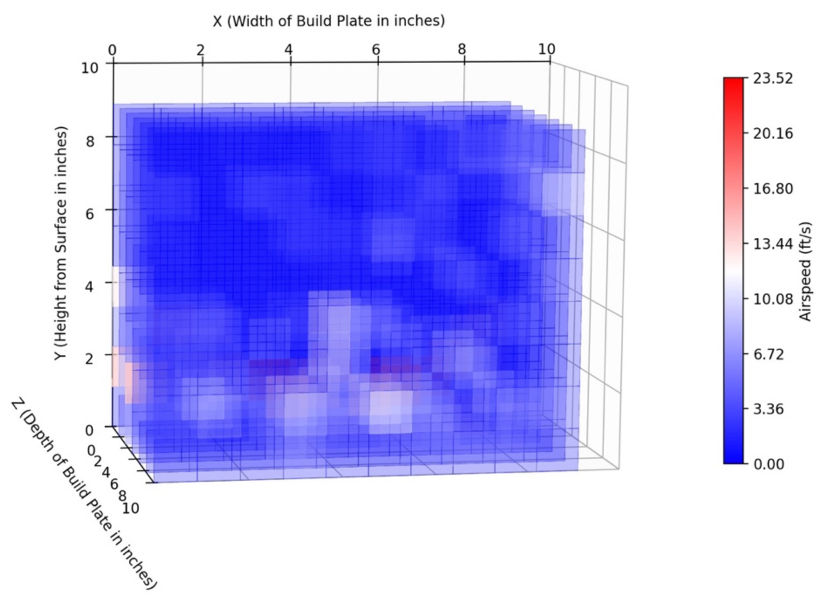

Figure 23. 3D airflow distribution across build plate (high flow)

To provide simplicity to the analysis of the airflow results, 4 critical points were chosen across the build plate where the most notable changes to the airflow were observed. Those critical points were at the front edge of the build plate (increment 1), just in from the front edge (increment

2), the middle of the plate (increment 5), and the rear edge (increment 10). Increments 1 and 10 were chosen to show the initial and final flow characteristics of the airflow across the build plate. Increment 2 was selected to examine the effects of the growing stagnant zone, as shown in the manufacturer's CFD, just inside the front edge of the build plate. Increment 5 was chosen as it showcases the transition of the front half of the build plate onto the back half, a change that resulted in a streamlining of the flow conditions from the turbulent flow seen in the front half. The four critical stages will be examined in the following sections.

5.1 Critical Point 1

The first critical point to examine in the chamber is the leading edge of the build plate. This point represents the vertical plane that extends up from the front of the build plate and provides the initial conditions of the airflow as it enters the direct print area. The CFD provided by the manufacturer is again shown below, highlighting the critical point 1 area in pink.

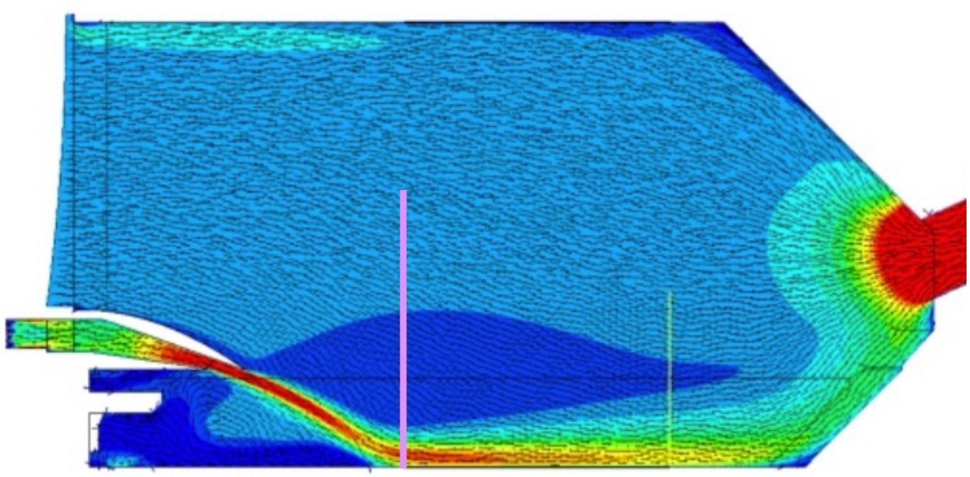

Figure 24. Critical point 1 manufacturer CFD diagram [10]

In Figure 24, there is a steep decline in the airflow plate as the flow is directed onto the build plate. A dark red flow line showcasing high-velocity flow directly off the surface of the flow ramp is observed. The strong flow towards the surface results in a stagnant flow zone forming directly over the leading edge of the build plate.

5.1.1 Nominal Airflow

Figure 25 below showcases the airflow data measured at nominal airspeed at the leading edge of the build plate (Z-Increment = 1).

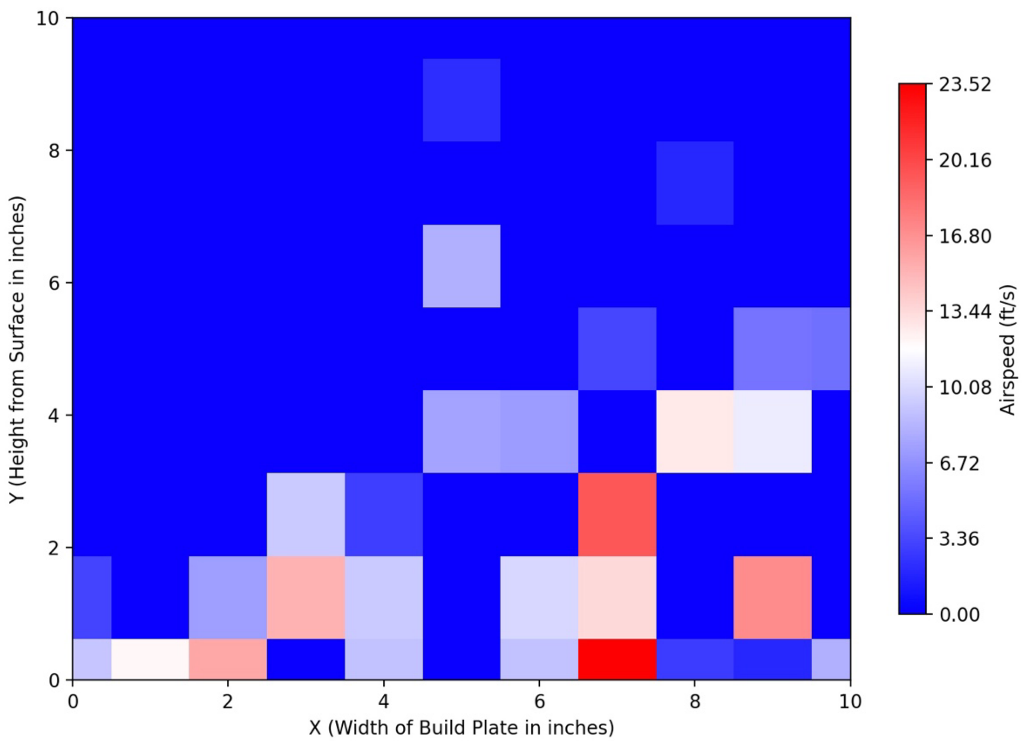

Figure 25. Airflow distribution at critical point 1 (nominal flow)

As seen in Figure 25, the airflow enters the build plate volume with higher velocities (warmer colors) closer to the surface of the plate. In contrast, 4 inches above, a stagnant flow zone (cooler colors) can be observed, with almost all values near or at 0 ft/s. A stronger flow stream is seen on the right side of the plate, reaching almost 6 inches above the surface of the plate, while the left side struggles to reach 2 inches. Minor channels can be seen in the upper half of the measurement plane; this may be a result of pitot tube measurement discrepancies, as non-normal flow will be read as stagnant (v=0 ft/s).

5.1.2 Low Airflow

Figure 26 below showcases the airflow data measured at low airspeed at the leading edge of the build plate (Z-Increment = 1).

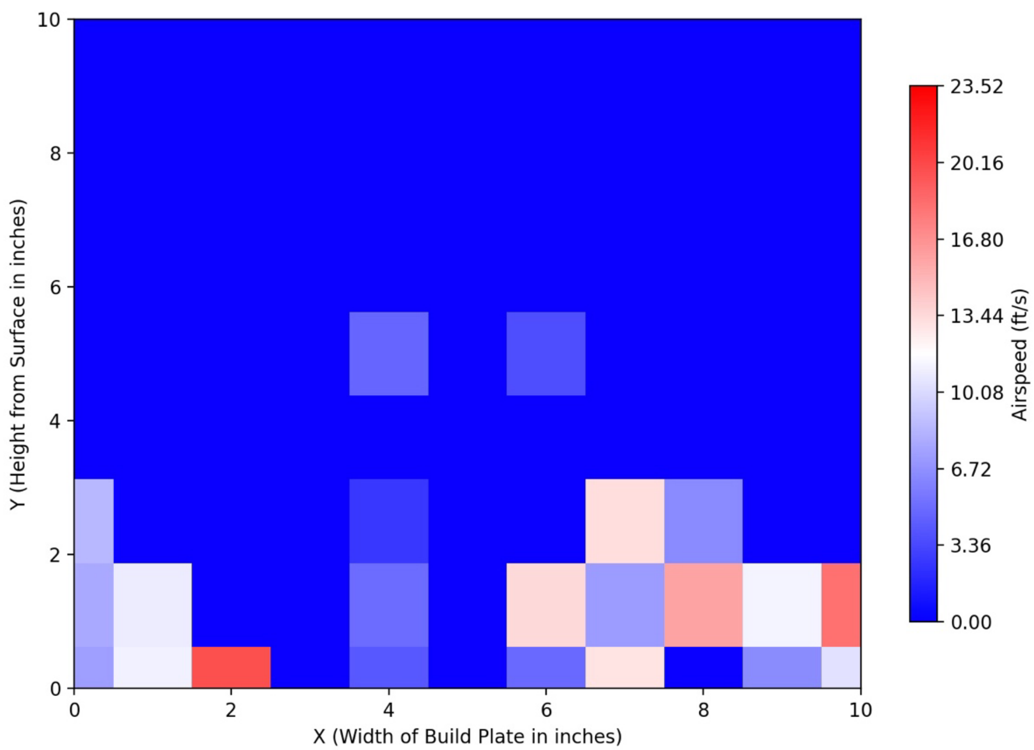

Figure 26. Airflow distribution at critical point 1 (low flow)

Figure 26 shows that with a decrease in flow velocity, even of only 0.10 m/s (0.33 ft/s), the flow entering the build plate zone is greatly affected. A stronger right channel is still observable in this figure, however with much less momentum, reaching a maximum height of 3 inches, albeit very weak at that height. This figure could suggest not enough momentum behind the flow to keep it stuck to the guide ramp, resulting in a turbulent, swirling flow at the front of the chamber.

5.1.3 High Airflow

Figure 27 below showcases the airflow data measured at high airspeed at the leading edge of the build plate (Z-Increment = 1).

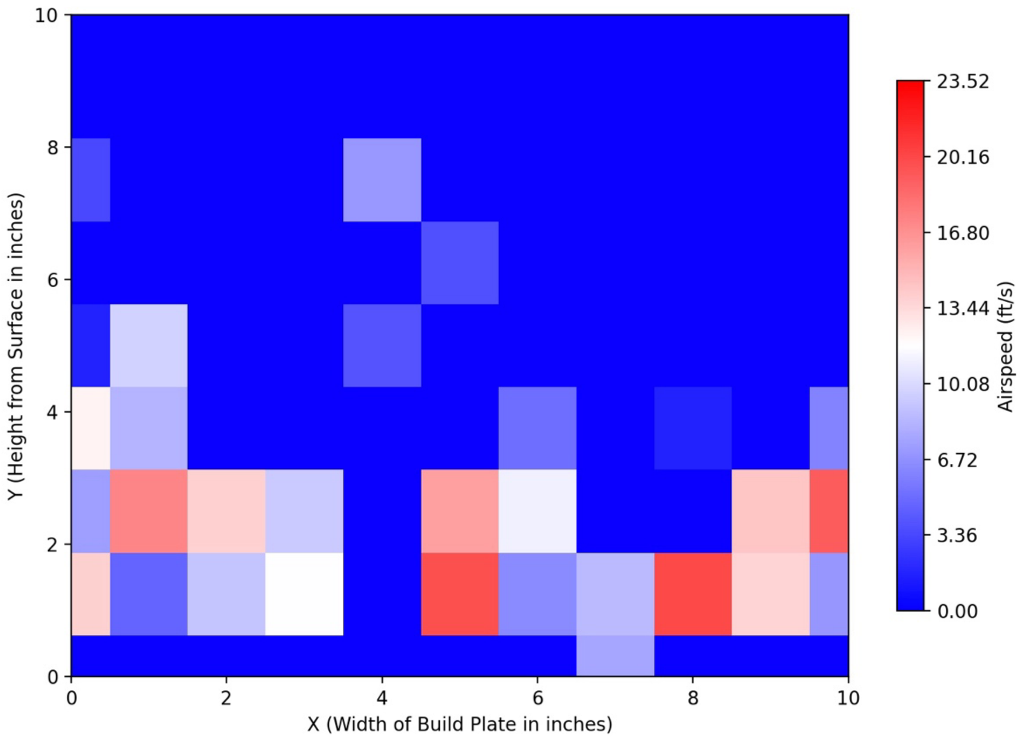

Figure 27. Airflow distribution at critical point 1 (high flow)

For high flow, contrary to low flow, there is evident flow momentum as it reaches the leading edge of the build plate. The more vibrant red colors suggest a more consistent increased velocity in the 1-4-inch range above the build plate surface. There is a flow gap observed in the 0-0.75-inch height mark. This gap presents an opposite idea from low flow, which is that with so much momentum behind the flow its streamline can push further out into the center of the chamber preventing it from curving down to the surface, as seen from nominal flow. This would suggest that nominal flow is within reasonable accuracy of manufacture CFD, while low and high flow follow predictable trends as they enter the build plate volume.

5.2 Critical Point 2

The second critical point of the chamber to be examined is just after the leading edge of the build plate. This point represents the vertical plane extend up 1-inch onto the build plate from the front edge and provides the conditions of the airflow as it crosses over the first specimens. The manufacturer CFD is again provided below, highlighting the critical point 2 area in pink. Critical point 2, although directly after the previously examined first point, showcases a noticeable deceleration of the airflow and increased stagnant zone. As discussed previously, however, due to pitot tubes only measuring flow that is normal to it, this stagnant flow most likely represents a turbulent, swirling flow.

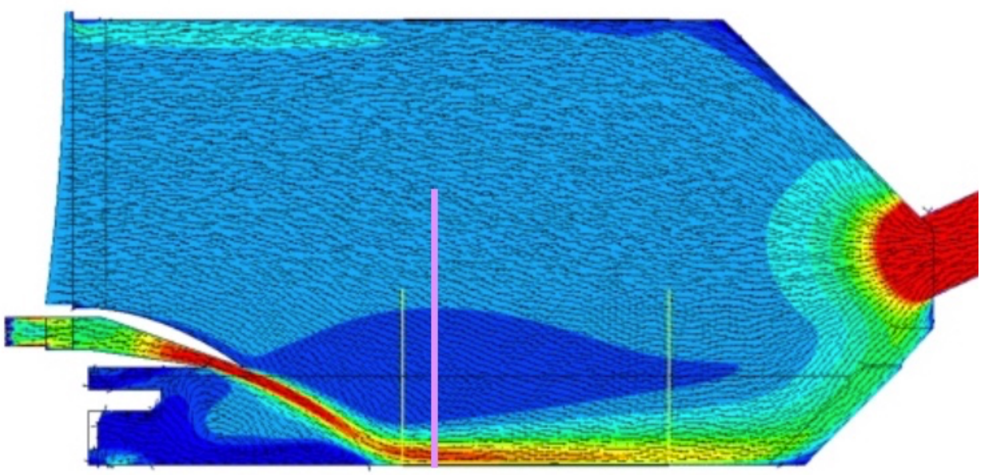

Figure 28. Critical point 2 manufacturer CFD diagram [10]

5.2.1 Nominal Airflow

Figure 29 below showcases the airflow data measured at nominal airspeed just after the leading edge of the build plate (Z-Increment = 2).

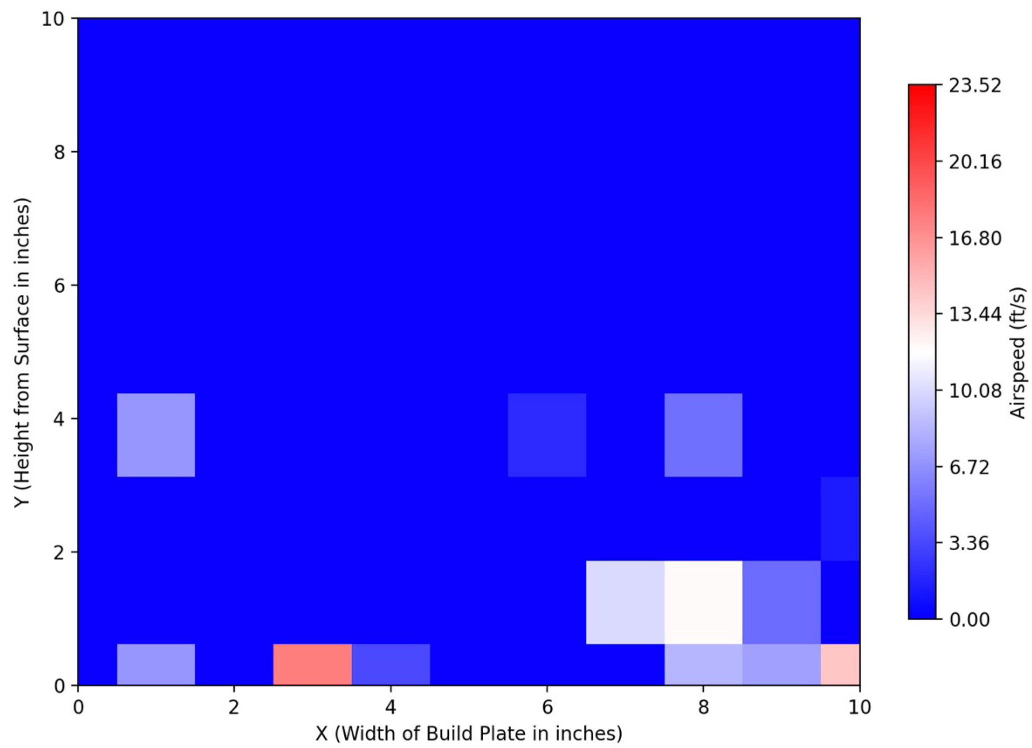

Figure 29. Airflow distribution at critical point 2 (nominal flow)

Figure 29 presents a very weak airflow not only over the build plate surface but also over the entire measurement plane. Not only is the stagnant zone observable from this figure, but it is also exacerbated, as it captures all but roughly thirteen scan points, with only three showing above-average flow velocities.

5.2.2 Low Airflow

Figure 30 below showcases the airflow data measured at low airspeed just after the leading edge of the build plate (Z-Increment = 2).

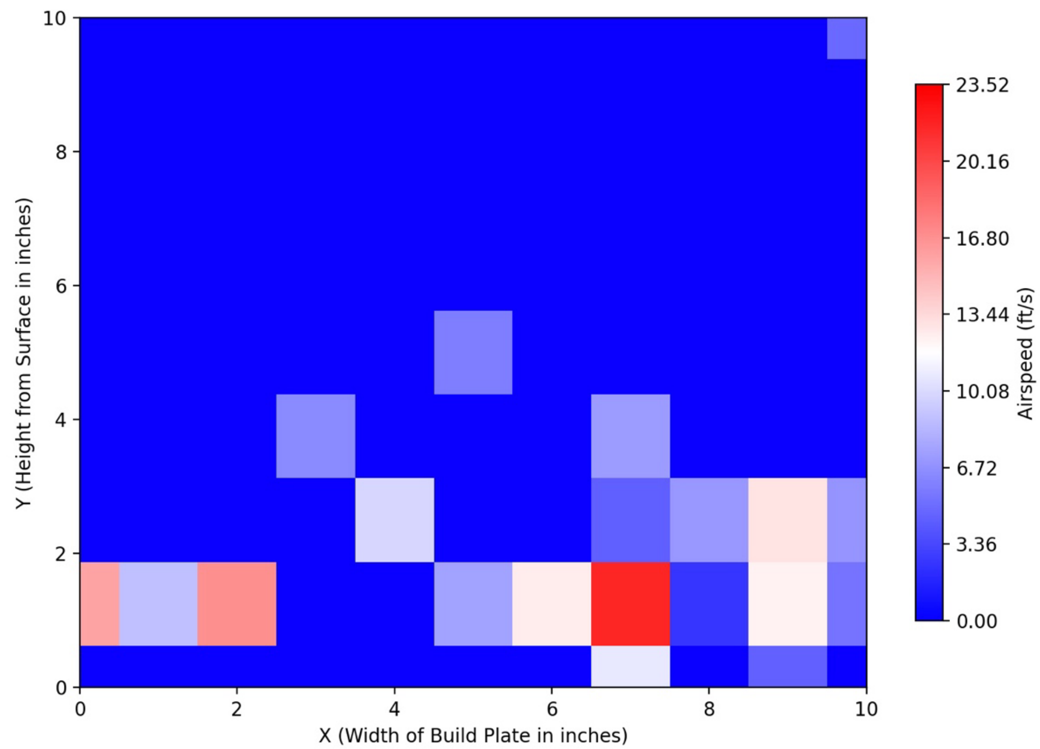

Figure 30. Airflow distribution at critical point 2 (low flow)

At increment 2, an increase in flow velocity can be seen across the surface of the build plate. Contrary to nominal flow, this results in the flow lining up with the manufacturer's CFD much more than at critical point 1. Similar to critical point 1, there is still an observable flow channel on the right side of the chamber.

5.2.3 High Airflow

Figure 31 below showcases the airflow data measured at high airspeed just after the leading edge of the build plate (Z-Increment = 2).

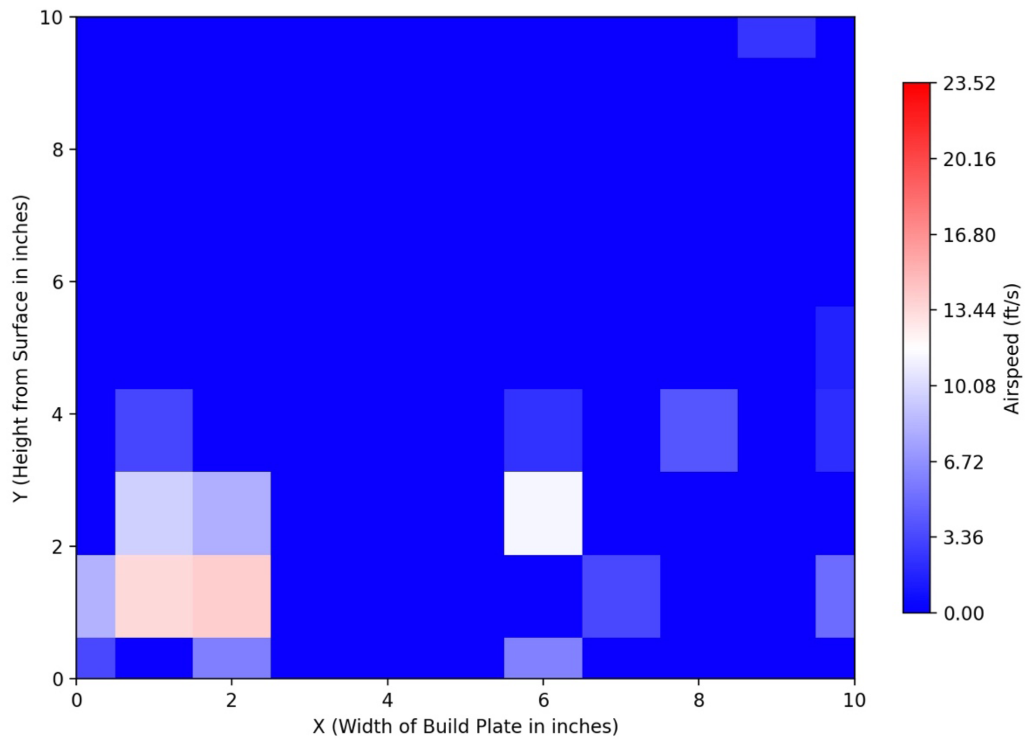

Figure 31. Airflow distribution at critical point 2 (high flow)

Consistent with nominal flow, the high flow distribution seems to decrease at critical point 2 significantly. Interestingly, consistent with critical point 1, high flow has an evident flow channel that favors the left side of the chamber, opposite to the other flow conditions. Although this condition presents the highest intended flow velocity, this figure presents the lowest maximum flow velocity through this critical point.

5.3 Critical Point 3

The third critical point to examine in the chamber is the centerline of the build plate. This point represents the vertical plane extending up in the middle of the build plate and provides the second-half transitional airflow conditions. The CFD provided by the manufacturer is again shown below, highlighting the critical point 3 area in pink. It is at this point that the stagnant zone begins to tail off, and the surface flow loses considerable velocity and begins to detach from the plate.

This would suggest enough of a decrease in velocity to reduce a skin friction boundary flow from the surface.

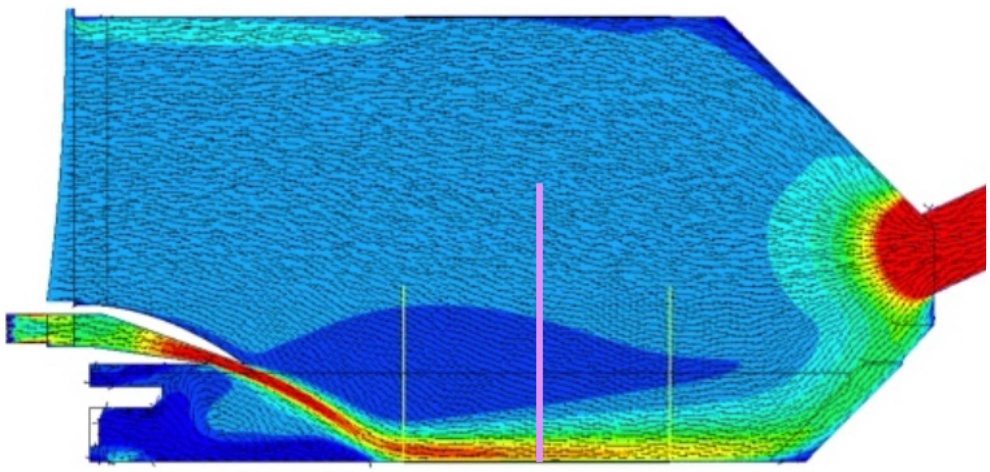

Figure 32. Critical point 3 manufacturer CFD diagram [10]

5.3.1 Nominal Airflow

Figure 33 below showcases the airflow data measured at nominal airspeed at the centerline of the build plate (Z-Increment = 5).

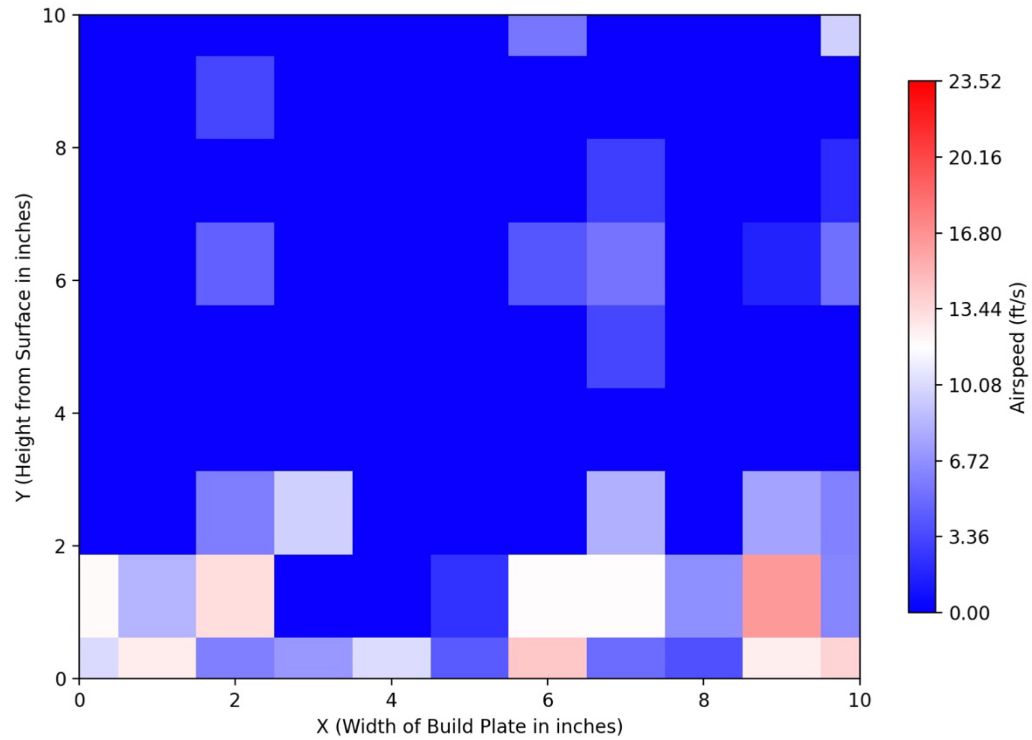

Figure 33. Airflow distribution at critical point 3 (nominal flow)

As seen in Figure 33, the nominal flow begins to level out at the surface at the centerline of the build plate. More consistent coloring indicates an average velocity flow that spans most of the plate's width. The right-side channel is present; however, it has become less significant. At this stage, there is also more visible streamline flow in the upper half of the measurement plane. This is important as the upper stream plays a vital role in carrying spatter out of the print zone quickly, preventing damage to the laser lenses.

5.3.2 Low Airflow

Figure 34 below showcases the airflow data measured at low airspeed at the centerline of the build plate (Z-Increment = 5).

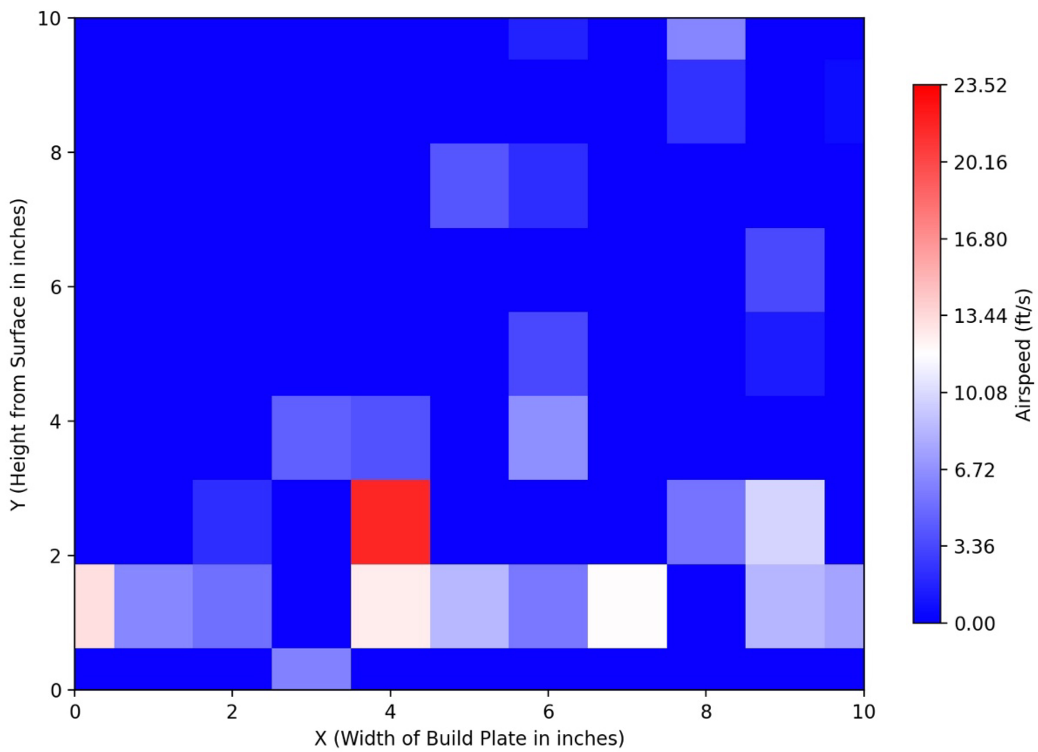

Figure 34. Airflow distribution at critical point 3 (low flow)

Low velocity airflow shows a similar pattern to nominal flow; however, much like at stage one, its flow suggests significantly weaker momentum. This could be attributed to the effects of low flow never establishing an initial flow pattern, resulting in a gentler turbulent stream that is now beginning to level out, albeit with lower velocities.

5.3.3 High Airflow

Figure 35 below showcases the airflow data measured at high airspeed at the centerline of the build plate (Z-Increment = 5).

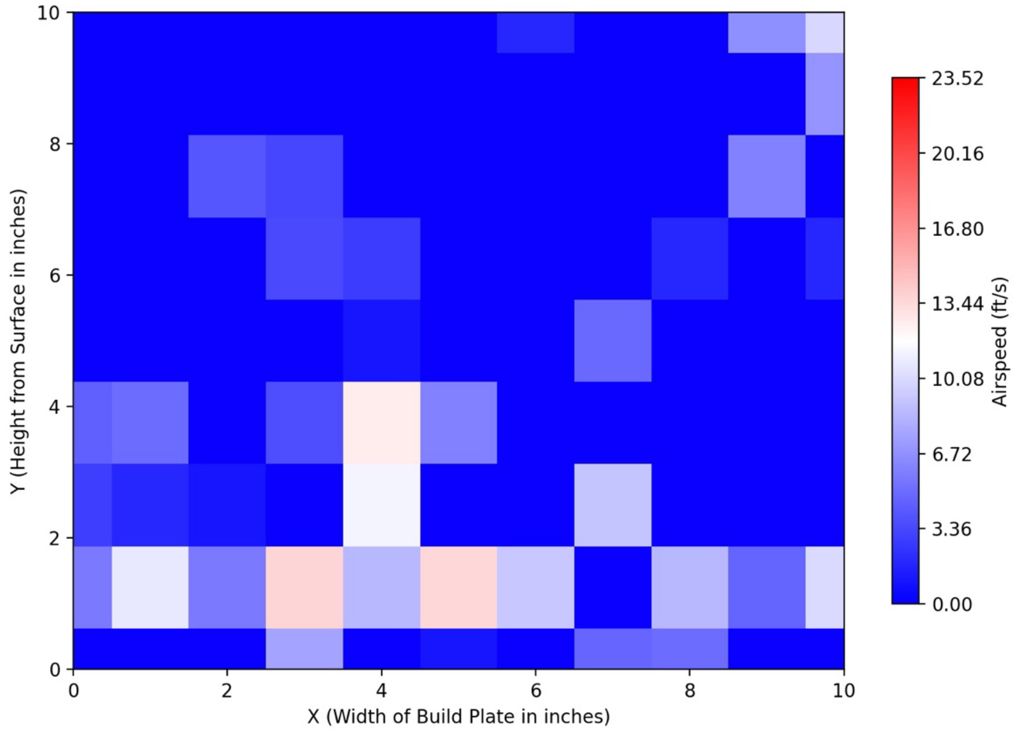

Figure 35. Airflow distribution at critical point 3 (high flow)

High-velocity flow showcases a more consistent flow pattern than that provided in the manufacturer's CFD, with a strong lower flow that decreases in velocity as it drifts up from the surface. The left channel remains observable, albeit faintly – much like the other two conditions. The splatter-like distribution of high-velocity points raises concerns of turbulent flow above the surface of the build plate, as there are high points rather than larger channels. This suggests the possibility of swirling flows that are normal to the pitot tube at single points, giving the illusion of micro-channels; however, further airflow analysis that encapsulates the flow characteristics from several directions would be needed to confirm.

5.4 Critical Point 4

The fourth critical point to examine in the chamber is the trailing edge of the build plate. This point represents the vertical plane extended up on the rear edge of the build plate and represents the final airflow conditions as the flow exits the plate area. The manufacturer's CFD is provided below again, highlighting the critical point 4 area in pink. At this point, the flow is quickly climbing to the exit of the chamber, with very little stagnant zone remaining. From the CFD below, there appear to be four distinct velocity levels rising from the surface, which is quite different from the initial commanding channel seen at critical point 1.

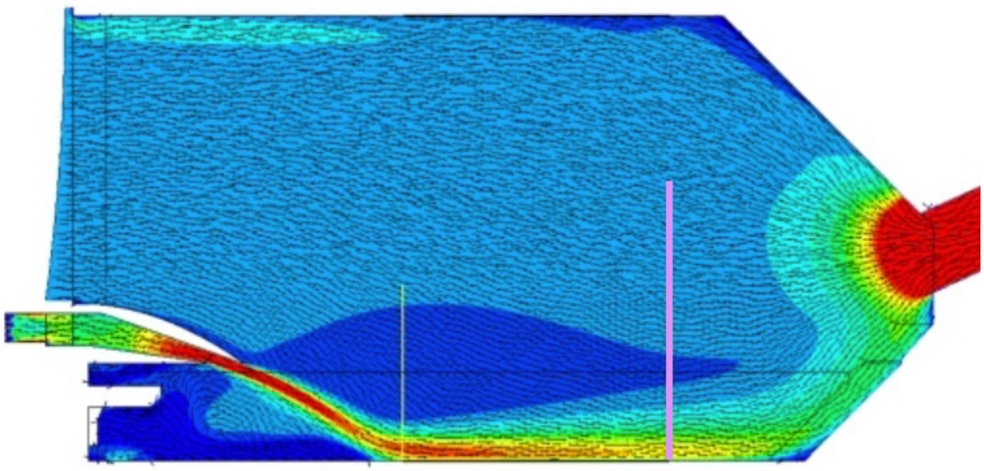

Figure 36. Critical point 4 manufacturer CFD diagram [10]

5.4.1 Nominal Airflow

Figure 37 below showcases the airflow data measured at nominal airspeed at the trailing edge of the build plate (Z-Increment = 10).

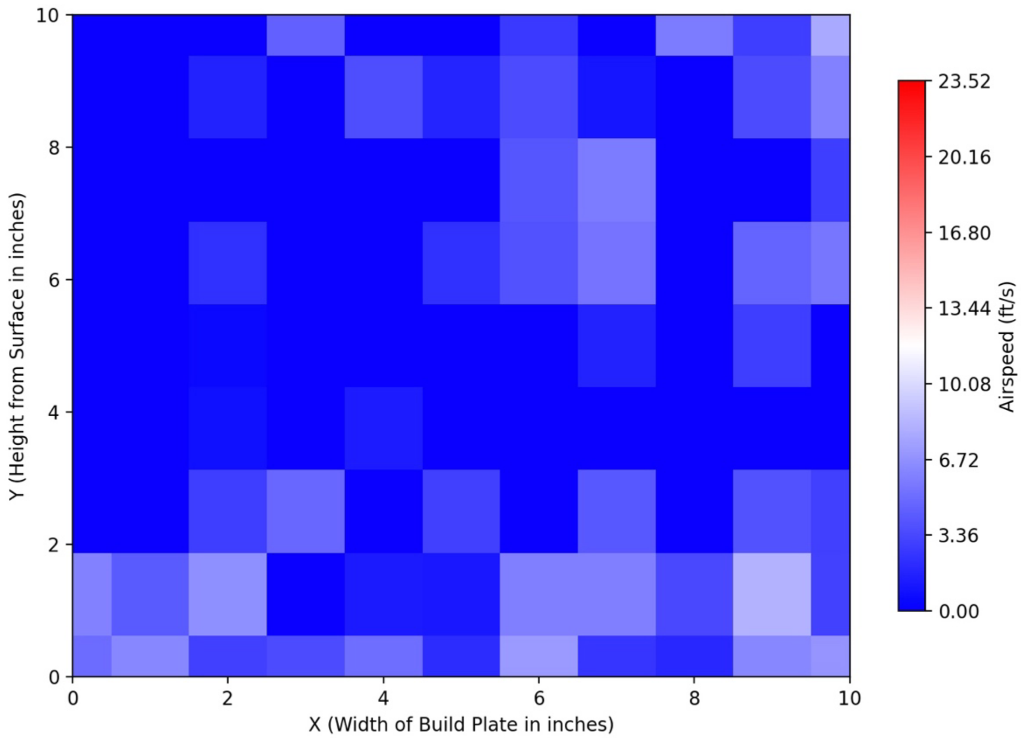

Figure 37. Airflow distribution at critical point 4 (nominal flow)

At critical point 4, the nominal flow can be shown lifting off the surface and heading for the exit port. There is also a consistent, yet lower velocity, flow maintained across the surface of the build plate. The increased flow channel on the right side of the chamber has bled into the surrounding area, resulting in a more pronounced dead channel on the left side than a strong one on the right. This consistent favoring of the right side is of significant note, as it has maintained consistency through other flow changes across all four points.

5.4.2 Low Airflow

Figure 38 below showcases the airflow data measured at low airspeed at the trailing edge of the build plate (Z-Increment = 10).

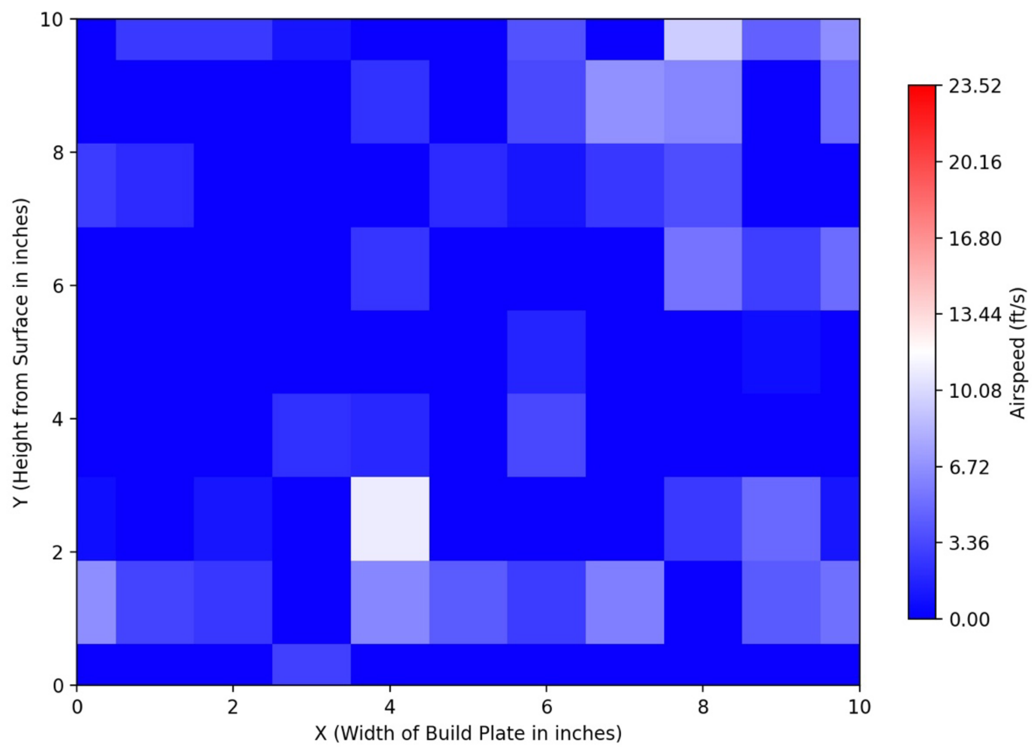

Figure 38. Airflow distribution at critical point 4 (low flow)

Low velocity flow shows a similar trend to that of nominal flow as it is more evenly distributed across the entire plane. Interestingly, a reverse effect of high velocity critical point 1 can be observed at the surface of the plate where the 0-~0.75-inch height range is consistently 0 ft/s across the width of the build plate. Inversely to critical point 1 and high flow, this suggests that the low velocity of the flow is easily pulled off the surface of the plate and towards the exit port. The right-side channel can still be observed, albeit lifted in the plane, suggesting an effect from the exit port.

5.4.3 High Airflow

Figure 39 below showcases the airflow data measured at high airspeed at the trailing edge of the build plate (Z-Increment = 10).

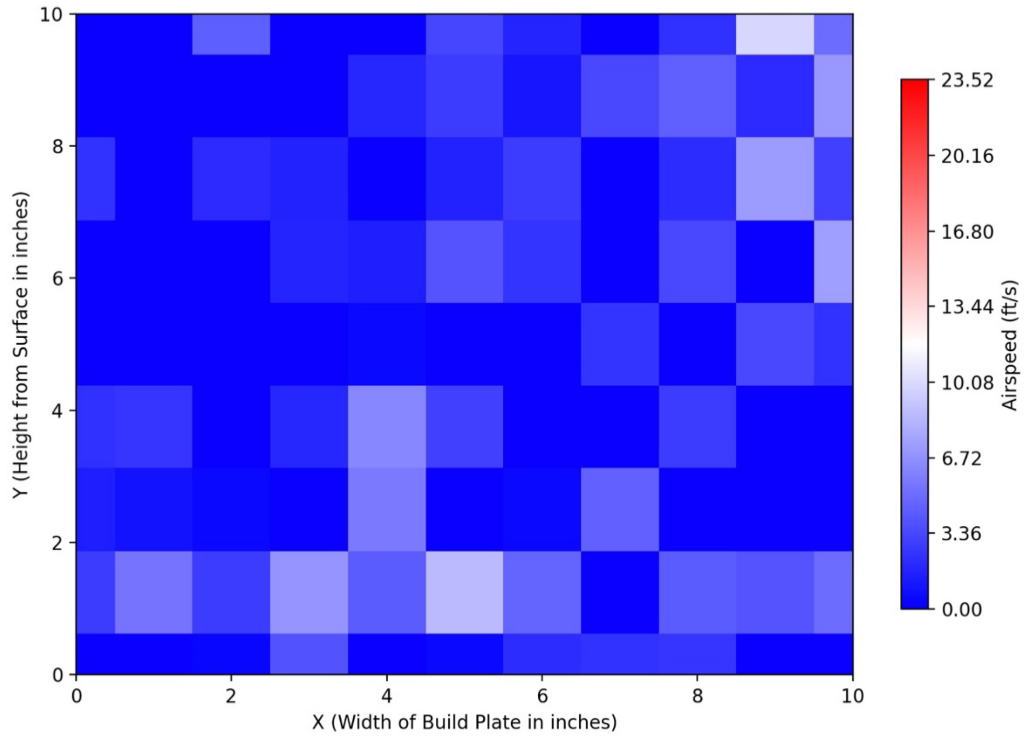

Figure 39. Airflow distribution at critical point 4 (high flow)

High-velocity airflow provides the most variation across the measurement plane at critical point 4. It is at this point that the flow can showcase some level of consistency for multiple measurement points in an area, suggesting that it may require the entire build plate for the initial force of the high velocity to regulate into streamlines. Interestingly, the consistent left side channel that opposed the nominal and low right side channels has now shifted to the upper right side of the measurement plane, suggesting there may be a strong pull to that corner that all three flows experience. There is again a lack of consistent flow at the surface of the build plate, suggesting that the high flow never fully influences the surface of the prints – a critical area in the process.

5.5 Airflow Statistical Comparisons

Table 4 below provides the statistical data from the four critical points in terms of velocity data, all given in ft/s.

Table 3. Statistical comparison of airflow data

Stage	Low			Nominal			High		
	Average (ft/s)	Std Dev.	Max (ft/s)	Average (ft/s)	Std. Dev.	Max (ft/s)	Average (ft/s)	Std. Dev.	Max (ft/s)
1	2.0852	4.506	19.78	2.6271	5.062	23.52	2.9706	5.379	20.12
2	1.8625	4.305	21.72	1.0095	3.105	17.65	1.0538	2.831	13.98
5	1.6617	3.657	21.77	2.8240	4.403	16.39	2.2311	3.640	13.63
10	1.6130	2.366	10.89	2.4904	3.307	12.29	1.9500	2.272	9.900

The table above pulls all the figures into one numerical analysis, allowing for side-by-side comparison of each flow condition. The most ideal velocity is shaded green while least ideal is shaded red, yellow represents the middle value. For critical point 1, low velocity presents uniform least-ideal data while high commands all but maximum value. The values are nearly evenly spaced, all with high standard deviations, showing that this stage is by far the most inconsistent for all conditions. Critical point 2 presents interesting data as low flow velocity showcases uniform ideal conditions, pointing to the previously mentioned flow-control that the lower velocity/pressure provided, whereas the other two conditions may be affected by more turbulent flow. It is important to note that although less ideal flow conditions for nominal and high, their standard deviations present significantly more uniform data than low velocity. For critical points 3 and 4 the data tends to similar conclusions of each other. Nominal flow velocity contains the highest average flow for 3 and 4, however with the highest deviation values, which can be seen in the strong presence of channels in the figures. Low flow velocity presents the lowest average flow velocity, as expected, with average standard deviation values. High flow velocity, interestingly, provided the lowest maximum values for both critical points. This could be a factor of the highly turbulent flow present in the rear of the chamber at this condition.

Overall deviations between data from each condition were minimal, however the trends must be analyzed against expectations. Low airflow, overall, performed as expected with 75% of the lowest flow velocity means, whereas nominal and high velocity did not. High airflow, although turbulent in sections, was most evenly distributed, accounting for 75% of the ideal standard deviations. Low airflow, although the lowest inlet velocity, accounted for half of the maximum values, however they were across the two center points, performing poorly on the edges. These numbers support a finding that although each airflow condition exhibits ideal traits in specific categories and build plate locations, none of them perform uniformly ideally or as fully expected.

5.6 Comparison of Flow and Strength Characteristics

As stated previously, this thesis looks to compare the collected airflow data to mechanical testing previously completed by Joshua Hall at the SAML utilizing these same GE Concept 2 printers. In Mr. Hall's study, a comparison was conducted against airflow, laser energy and scan speed. These comparisons looked at how different combinations of these factors resulted in differing mechanical properties, namely Ultimate Tensile and Yield Tensile Strength, as previously mentioned. Shown in the figure below is a visualization of the strength comparisons for all twenty-one (21) conditions tested. For the purposes of this thesis, only the airflow velocity (L, N, H) and strength values will be analyzed, as scan speed (V) and laser power (LP) were not utilized during the measurement process.

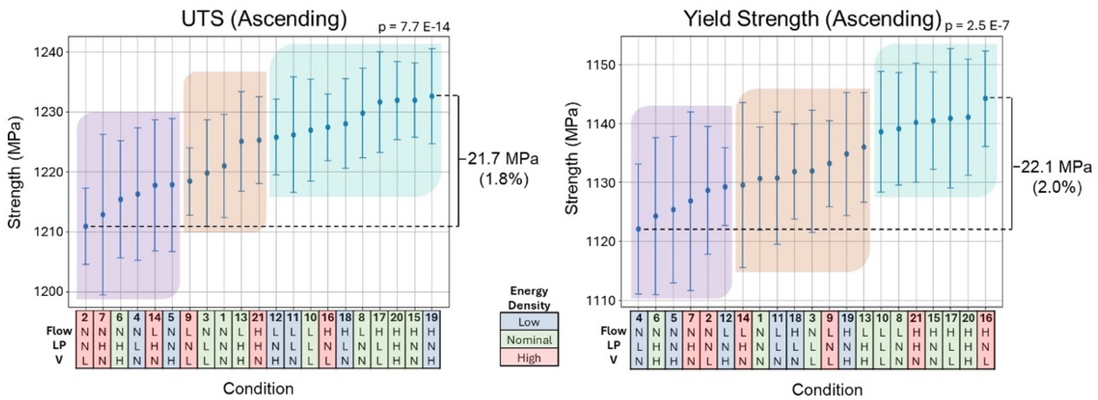

Figure 4. Comparison of the means and standard deviations of (a) UTS and (b) Yield Strength for each condition, split into thirds based on the difference between the highest and lowest means.

Figure 40. Strength results extracted from Mr. Hall's study [21]

Although there are many varying factors that don't provide a clear-cut picture on a strength tier regardless of LP or V values, nominal airflow consistently ranked in the lower third for strength. Low and High airflow are scattered throughout the upper two-thirds; however high-flow has a higher average strength value regardless of other conditions. This would suggest, that on average, regardless of other conditions, the data tends towards a strength ranking of: High, Low and Nominal flow, greatest to least strength, respectively. It is important to note, however, that the range for these differences is approximately 22 MPa, or roughly 2.0% of the total strength.

Chapter 6. Conclusions and Future Work

The data collected and analyzed in this thesis provides a pivotal insight into the airflow characteristics in the LPBF process. Overall, the airflow tends towards the flow characteristics of the manufacturer provided CFD. It is evident through the figures and flow statistic table that the airflow is affected by the manipulation of the input velocity, however the trends are not consistent in favoring one flow velocity over the others. Generally, the high velocity flow resulted in cleaner distributions, but with lower average flow velocities – likely a result of turbulent flow. The low flow velocity showcased a more stagnant flow across the entire chamber, except for at critical points 2 and 3 where it showcases maximum flow points against the other two conditions. Nominal flow followed the trends of the manufacturer CFD and showcased a steadier mean flow velocity throughout, however with the highest variance across the plane. This results in the inability to conclude one flow condition as the most/least ideal for printing as the only manipulated variable.

The mechanical testing data showcased similar results to that of the airflow. Although the strengths tended towards a ranking of nominal -> low -> high, least to greatest strength, the variation was roughly only 2.0%, as previously mentioned. This small variance can be generally regarded as insignificant, however further research is needed into the statistical impact of the variance on the mechanical strength differences.

The channels presented in the airflow figures suggest build plate zones of more ideal print qualities that should be further researched for ideal part placements during sensitive printing. Further research should also be conducted on the orientation of sensitive parts as faces on the side of airflow input will inherit higher quality flow than those on the backside. This phenomenon should also be further researched to examine how the introduction of printed parts affects the overall airflow across the plate as this testing was completed with a blank plate. Further examination into the effects of flow from non-normal directions should also be taken into consideration as, for the purposes of this thesis, stagnant flow is viewed as “poor” however, it could result in ideal flow around the complex geometry of parts as a vortex – helping air reach the backsides.

Overall, this thesis should be used as a guide to help better understand the flow characteristics and print qualities. For sensitive component manufacturing, such as that found in aerospace and defense operations, further research should be conducted post-processing to ensure proper qualifications. This should include confirmation of mechanical strengths, surface qualities and fatigue lifespans, using statistically significant test specimens to confirm all theoretical assumptions. Multiple sources of validation must be performed to properly certify sensitive parts and continues to be a limiting factor in advanced manufacturing practices. Due to this, further research efforts must receive proper support and consideration to continue innovating.

6.1 Sources of Error and Difficulty

The leading source of error in this testing was the limited airflow measurement capability. Due to pitot tubes only being able to measure flow that is normal to them, many points were measured as zero and provided no meaningful data. This caused many points to appear as stagnant flow zones when they could have been places of vortices that were undetectable. Another source of difficulty while analyzing the chamber was the size constraint due to the geometry of the interior chamber. This resulted in many iterations and manipulations to be made to the device during the design phase and while testing to ensure proper fit and as accurate results as possible.

6.2 Future Impacts

With initial airflow measurements obtained and visualized, future print analyses can now be compared and studied from a broader scope. Prints that require more specific airflow characteristics can be placed in specific locations of the plate that maintain higher and more consistent airflow, such as the right channel for low and nominal flow, and the left channel for high flow. Although this is the first non-CFD airflow analysis completed on a printer at the SAML, it provides meaningful data that will immediately impact decisions. The next steps to build on this research would be to incorporate a broader scope of airflow measurements that followed the entire path of the flow from entrance to exit and examine the flows from the sides more accurately to identify stagnant and vortices zones. Flow must also be considered for conditions that contain a part within the printer as this will greatly affect flow conditions.

References

[1] "3D Printing Cost and Speed: Trace the Evolution and Calculate with UnionFab," UnionFab – 3D Printing; 2023.

[2] R. J. N. Joshua, et. al, "Powder Bed Fusion 3D Printing in Precision Manufacturing for Biomedical Applications: A Comprehensive Review," *Materials*, vol. 17, no. 3, 2024.

[3] V. Alcacer and V. Cruz-Machado, "Scanning the Industry 4.0: A Literature Review on Technologies for Manufacturing Systems," *Engineering Science and Technology, an International Journal*, vol. 22, pp. 899–919, 2019.

[4] A., Bidare, et al. "Powder-bed laser hybrid additive manufacturing of metals: A review – The International Journal of Advanced Manufacturing Technology," *SpringerLink* Available: https://link.springer.com/article/10.1007/s00170-021-06855-4.

[5] "Laser Powder Bed Fusion (LPBF) - MET3DP," *Metal3DP* https://met3dp.com/lpbf-202404234/.

[6] Z. Guoqing, et. al, "Optimized design and key performance factors of a gas circulation filtration system in a metal 3D printer," *Scientific Reports*, vol. 12, 2022.

[7] A. Ladewig, G. Schlick, M. Fisser, V. Schulze, and U. Glatzel, "Influence of the shielding gas flow on the removal of process by-products in the selective laser melting process," *Additive Manufacturing*, vol. 10, pp. 1–9, 2016.

[8] J. Yin *et al.*, "Correlation between forming quality and spatter dynamics in laser powder bed fusion," *Additive Manufacturing*, vol. 31, 2020.

[9] C. Qingpen, et. al, "Effect of laser powder bed fusion gas flow rate on microstructure and mechanical properties of 316 L stainless steel," *Journal of Manufacturing Processes*, vol. 132, pp. 850–862, 2024.

[10] Dr. B. Roidl and T. Fauner, "Continuous Improvement in Gas Flow Design," *GE Additive*, 2021.

[11] "Reverse engineering," Legal Information Institute, https://www.law.cornell.edu/wex/reverse_engineering#:~:text=Reverse%20engineering%20means%20a%20method,U.S.%20470%20(1974)%20).

[12] USAF, "B-52H Stratofortress," Air Force, https://www.af.mil/About-Us/Fact-Sheets/Display/Article/104465/b-52h-stratofortress/#:~:text=The%20Air%20Force%20currently%20expects,Air%20Command%20in%20May%201961.

[13] W.-Y. Chang, J.-W. Hsu, and B.-Y. Hsu, "3D Scanning System of Structured Light for Aiding Workpiece Position of CNC Machine Tool," *2018 IEEE International Conference on Advanced Manufacturing*, 2018.

[14] M. Javaid, et. al, "Different Flexibilities of 3D Scanners and Their Impact on Distinctive Applications: An Analysis," *International Journal of Business Analytics*, vol. 7, no. 1, 2020.

[15] A. Haleem *et al.*, "Exploring the potential of 3D scanning in Industry 4.0: An overview," *International Journal of Cognitive Computing in Engineering*, vol. 3, pp. 161–171, 2022.

[16] Keyence, "VL Series Scanners," KEYENCE, https://www.keyence.com/products/3d-measure/3d-scanner/vl-800/lp/186082001.jsp?aw=google-kaenVL696129pp-br&gad_source=1&gad_campaignid=1723616848&gbraid=0AAAADlj0X6ft2-BsK-Icxw0PNt7qP64u&gclid=CjwKCAjwiezABhBZEiwAEbTPGKZzudHR-7MYlZO49LhCD3_gjDF5kXBxFMKPCmcZDB2UpnzZb8GmCxoCzL4QAvD_BwE

[17] "Revopoint MetroX Laser Scanner: Blue Laser Line & Full-field structured light 3D scanner," *Revopoint 3D US* Available: https://www.revopoint3d.com/products/3d-laser-scanner-metrox?msged=1.

[18] Jiménez, A., Bidare, P., Hassanin, H. et al. "Powder-based laser hybrid additive manufacturing of metals: a review" International Journal of Advanced Manufacturing Technology. Vol. 114, pp. 63–96 (2021). https://doi.org/10.1007/s00170-021-06855-4

[19] "LabJack T7-Pro," LabJack, https://labjack.com/products/labjack-t7-pro?srsltid=AfmBOoon4tS3JZ8zEWGQzxqmaGGtj7Zfq6mdPh8YfFDnD8KVSNB_5TLT (accessed May 20, 2025).

[20] Dang, N. Hung; et al. "A critical review on additive manufacturing of Ti-6Al-4V alloy: microstructure and mechanical properties" Journal of Materials Research and Technology. Vol. 18. Pp. 4641-4661. May-June 2022

[21] Hall, Joshua D, "Influence of Minor Print Parameter Variations on the Mechanical Properties of Additively Manufactured Ti-6Al-4V Parts Using Laser Powder Bed Fusion

[22] ASTM "Standard test methods for tension testing of metallic materials," American Society for Testing and Materials *E8/E8M*

[23] Fouda, Moateasem;"*Figure 1 dogbone specimen for tensile testing (dimensions in mm)."* Available: https://www.researchgate.net/figure/Dogbone-specimen-for-tensile-testing-dimensions-in-mm_fig1_232834571.

[24] S. Chowdhury, et. al, "Laser powder bed fusion: a state-of-the-art review of the technology, materials, properties & defects, and numerical modeling," *Journal of Materials Research and Technology*, vol. 20, pp. 2109–2172, 2022.

[25] W. Abd-Elaziem, et. al, “On the current research progress of metallic materials fabricated by laser powder bed fusion process: a review,” *Journal of Material Research and Technology,* vol. 20, pp. 681–707, 2022.

[26] J. Sun *et al.*, “Effect of shielding gas flow rate on cladding quality of direct laser fabrication AISI 316L stainless steel,” *Journal of Manufacturing Processes*, vol. 48, pp. 51–65, 2019.

[27] A. B. Anwar and Q.-C. Pham, “Selective laser melting of AlSi10Mg: Effects of scan direction, part placement and inert gas flow velocity on tensile strength,” *Journal of Materials Processes and Technology*, vol. 240, pp. 338–396, 2017.

[28] T. Varady, R. R. Martin, and J. Cox, “Reverse Engineering of Geometric Models - An Introduction,” *Computer-Aided Design*, vol. 29, no. 4, pp. 255–268, 1997.

[29] Defense Logistics Agency, “Reverse Engineering,” Defense Logistics Agency, https://www.dla.mil/Aviation/Offers/Engineering/Reverse-Engineering/#:~:text=Reverse%20Engineering%20is%20the%20process,the%20item%20functionally%20and%20dimensionally.